© 2020. Published by The Company of Biologists Ltd | Journal of Cell Science (2020) 133, jcs240374. doi:10.1242/jcs.240374

RESEARCH ARTICLE

Cardiolipin is required for membrane docking of mitochondrial ribosomes and protein synthesis

Richard G. Lee[1,2,3], Junjie Gao[4], Stefan J. Siira[1,2,3], Anne-Marie Shearwood[1,2], Judith A. Ermer[1,2], Vinzenz Hofferek[5], James C. Mathews[1,2,3], Minghao Zheng[4], Gavin E. Reid[5,6,7], Oliver Rackham[1,2,8,9,10] and Aleksandra Filipovska[1,2,3,9,10,11,*]

ABSTRACT

The mitochondrial inner membrane contains a unique phospholipid known as cardiolipin (CL), which stabilises the protein complexes embedded in the membrane and supports its overall structure. Recent evidence indicates that the mitochondrial ribosome may associate with the inner membrane to facilitate co-translational insertion of the hydrophobic oxidative phosphorylation (OXPHOS) proteins into the inner membrane. We generated three mutant knockout cell lines for the CL biosynthesis gene *Crls1* to investigate the effects of CL loss on mitochondrial protein synthesis. Reduced CL levels caused altered mitochondrial morphology and transcriptome-wide changes that were accompanied by uncoordinated mitochondrial translation rates and impaired respiratory chain supercomplex formation. Aberrant protein synthesis was caused by impaired formation and distribution of mitochondrial ribosomes. Reduction or loss of CL resulted in divergent mitochondrial and endoplasmic reticulum stress responses. We show that CL is required to stabilise the interaction of the mitochondrial ribosome with the membrane via its association with OXA1 (also known as OXA1L) during active translation. This interaction facilitates insertion of newly synthesised mitochondrial proteins into the inner membrane and stabilises the respiratory supercomplexes.

KEY WORDS: Mitochondrial membrane, Protein synthesis, Mitochondrial ribosomes, Cardiolipin

INTRODUCTION

Mitochondria are highly dynamic organelles that play crucial roles in a variety of cellular processes, including energy production, Ca^{2+} homeostasis, fatty acid metabolism and apoptosis (Vafai and Mootha, 2012). Mitochondria possess a double lipid membrane that creates a compartmentalised region of the cell where the specialised conditions required for ATP synthesis are provided (Kühlbrandt, 2015). These membranes are host to protein complexes involved in different aspects of mitochondrial function, including energy production, membrane morphology regulation and protein translocation (Cogliati et al., 2016). The unique morphology of the inner mitochondrial membrane is the result of invaginations called cristae that create a large surface area to facilitate the insertion of multiple different protein complexes, most notably the oxidative phosphorylation (OXPHOS) complexes that are required for ATP production (Schenkel and Bakovic, 2014).

The inner mitochondrial membranes possess a unique anionic phospholipid called cardiolipin (CL), which comprises ∼15% of total mitochondrial membrane phospholipids and supports the unique membrane structures of mitochondria and the protein complexes within them (Schenkel and Bakovic, 2014). CL maintains the integrity of the inner mitochondrial membrane, regulates the balance of mitochondrial fusion and fission, and supports the function of protein complexes involved in respiration and protein translocation (Ban et al., 2018; Osman et al., 2011). CL defects have been implicated in multiple diseases including Parkinson's disease and Barth syndrome (Barth et al., 1983; Ryan et al., 2018), although the exact pathological mechanisms remain to be determined.

Recently, evidence from cryo-electron microscopy (cryo-EM) structures of the mitochondrial ribosome (mitoribosome) has indicated that these ribonuclear protein complexes interact with the mitochondrial inner membrane via the mitochondrial ribosomal protein of the large subunit 45 (MRPL45) (Greber et al., 2014). The N-terminal portion of MRPL45 was found within the polypeptide exit tunnel and was released from the tunnel when the mitoribosome switched to an elongation mode suggesting that it may target mitoribosomes to the protein-conducting pore in the inner mitochondrial membrane (Kummer et al., 2018). This was supported by evidence that deletion of the N-terminal tail of MRPL45 reduced protein synthesis, but it remains unclear if this is required for association with the mitochondrial membrane and OXA1 (Kummer et al., 2018). Furthermore, the C-terminal region of MRPL45 has been shown to share a high degree of homology with inner membrane associated proteins TIM44 and Mba1 from *Saccharomyces cerevisiae* (Greber et al., 2014; Preuss et al., 2001; Weiss et al., 1999). The location of MRPL45 near the polypeptide exit tunnel of the mitoribosome has been hypothesised to position the nascent peptides in the optimal orientation to facilitate co-translational insertion into the newly synthesised respiratory complexes by insertase proteins like OXA1 (also known as OXA1L) (Kummer et al., 2018; Ott and Herrmann, 2010; Richman et al., 2014; Nargang et al., 2002; Thompson et al., 2018).

Recently, we showed that impaired mitochondrial gene expression and translation were accompanied by aberrant cristae morphology and reduced mitochondrial fusion (Perks et al., 2017,

[1]Harry Perkins Institute of Medical Research, QEII Medical Centre, Nedlands, Western Australia 6009, Australia. [2]ARC Centre of Excellence in Synthetic Biology, QEII Medical Centre, Nedlands, Western Australia 6009, Australia. [3]Centre for Medical Research, The University of Western Australia, QEII Medical Centre, Nedlands, Western Australia 6009, Australia. [4]School of Biomedical Sciences, University of Western Australia, Perth, Australia. [5]School of Chemistry, The University of Melbourne, Parkville, Victoria, 3010, Australia. [6]Department of Biochemistry and Molecular Biology, The University of Melbourne, Parkville, Victoria, 3010, Australia. [7]Bio21 Molecular Science and Biotechnology Institute, The University of Melbourne, Parkville, Victoria, 3010, Australia. [8]School of Pharmacy and Biomedical Sciences, Curtin University, Bentley, Western Australia 6102, Australia. [9]Curtin Health Innovation Research Institute, Curtin University, Bentley, Western Australia 6102, Australia. [10]Telethon Kids Institute, Northern Entrance, Perth Children's Hospital, 15 Hospital Avenue, Nedlands, Western Australia, Australia. [11]School of Molecular Sciences, The University of Western Australia, Crawley, Western Australia 6009, Australia.

*Author for correspondence (aleksandra.filipovska@uwa.edu.au)

A.F., 0000-0002-6998-8403

Handling Editor: Jennifer Lippincott-Schwartz
Received 9 October 2019; Accepted 12 June 2020

Journal of Cell Science (2020) 133, jcs240374. doi:10.1242/jcs.240374

2018). Although reduced translation rates have been previously reported in cells with aberrant cristae morphology (Almajan et al., 2012), the exact mechanism behind this is still unknown. To investigate the relationship between the mitochondrial inner membrane and mitochondrial protein synthesis, we have established knockout mouse NIH-3T3 cell lines for the *Crls1* gene, which encodes a key enzyme in CL biosynthesis that converts phosphatidylglycerol (PG) into CL (Chen et al., 2006; Houtkooper and Vaz, 2008). The cell lines showed a progressively aberrant mitochondrial morphology as CRLS1 production was reduced or lost. This aberrant morphology resulted in reduced or uncoordinated mitochondrial protein synthesis that stemmed from impaired formation of mature mitoribosomes. Additionally, we established that a key step in co-translational protein insertion is the formation of a stable interaction between the mitoribosome and OXA1, which is mediated by CL, and facilitates the formation of the respiratory chain supercomplexes (RCSs).

RESULTS

Reduced CRLS1 expression impairs mitochondrial network formation and fusion

To investigate how changes in the mitochondrial inner membrane could affect protein synthesis, we established model cell lines with progressively reduced CL content. Mutations in the CL synthase 1 gene, *Crls1*, have been shown to cause impaired cristae formation in *Caenorhabditis elegans* as a result of CL loss (Sakamoto et al., 2012). Therefore, we used CRISPR/Cas9 to knock out *Crls1* in mouse NIH-3T3 cells, severely reducing CL synthesis and consequently its content within mitochondrial membranes (Fig. 1). We established three cell lines where each of the four *Crls1* alleles in NIH-3T3 cells, which are typically tetraploid, were edited as follows: a cell line with two different 1 bp deletions and a 2 bp deletion ($Crls1^{KO1}$); a cell line with similar 1 bp and 2 bp deletions but also an allele harbouring a 2 bp substitution mutation ($Crls1^{KO2}$); and a cell line with an identical 2 bp deletion in all four alleles ($Crls1^{KO3}$) (Fig. 1A). We confirmed the mRNA levels of *Crls1* were significantly reduced in all three cell lines by performing quantitative reverse transcription PCR (qRT-PCR), ranging from 18% of *Crls1* mRNA remaining compared to controls in the $Crls1^{KO1}$ cells, to 44% and 6% *Crls1* mRNA remaining compared to controls in the $Crls1^{KO2}$ cells and $Crls1^{KO3}$ cells, respectively (Fig. 1B). All CRISPR-induced deletions resulted in frameshifts that result in premature translation termination in exon 2 of the seven-exon mRNA, which are predicted to induce nonsense-mediated decay (NMD), as well as truncate the majority of the length of the encoded protein. The $Crls1^{KO2}$ dinucleotide substitution mutant allele that is present along with the three knockout alleles in the $Crls1^{KO2}$ cell line, however, is predicted to induce a single valine to proline change at position 124 without truncating the protein, which could lead to low levels of functional protein. The level of *Crls1* mRNA reduction correlated well with the detected CL levels, quantified using the CL -binding compound Nonyl Acridine Orange (NAO); showing that CL was significantly reduced in all three cell lines (Fig. 1C).

NAO can weakly bind to other mitochondrial phospholipids (Petit et al., 1992), therefore we used nano-electrospray ionisation–field asymmetric ion mobility spectrometry–ultra high resolution/accurate mass spectrometry (nESI-FAIMS-UHRAMS) to identify and quantify the level of total and individual CL species in the three knockout cell lines compared to the wild-type cells. The lipidomic profiles showed that $Crls1^{KO1}$ and $Crls1^{KO3}$ cells lacked CL, and that CL levels were significantly decreased in the $Crls1^{KO2}$ cells to 78% of those in the $Crls1^{WT}$ cells (Fig. 1D; Fig. S1). To confirm that *Crls1* was lacking, we then rescued the loss of CL by expressing wild-type *Crls1* in the $Crls1^{KO3}$ cells, which significantly increased the levels of CL (Fig. 1D). This validated that the defect in CL biosynthesis was a direct consequence of the *Crls1* gene knockout (Fig. 1D; Fig. S2A). The CL profile of the $Crls1^{KO2}$ cells, where CL levels were reduced, indicated that the levels of shorter acyl chain length and more highly unsaturated containing precursor CL species were increased compared to those found in the $Crls1^{WT}$ cells (Fig. 1E; Fig. S1). $Crls1^{KO3}$ cells transfected with wild-type *Crls1* showed the greatest recovery of their shorter acyl chain length CL species but decreased recovery of the levels of longer chain length CL precursors (Fig. 1F; Fig. S1). This indicates that lower CL levels result in reduction of longer acyl chain length CL precursors, and rescuing CL levels causes increased accumulation of shorter acyl length CL precursors in an effort to produce the longer length CL species.

Altered mitochondrial morphology was observed with the loss of *Crls1* expression. An imbalance of mitochondrial fusion and fission, resulting in a decreased reticular appearance of mitochondrial networks was identified in response to reduced *Crls1* expression and CL content (Fig. 2A,B). As *Crls1* expression decreased, the mitochondrial network showed a decrease in connected tubular structures and an increase in discontinuous punctate granule structures, indicating impaired mitochondrial fusion and an aberrant mitochondrial network structure. The $Crls1^{KO2}$ cells, where CL levels were reduced, demonstrated a more intermediate morphological defect with both tubular and granular structures, potentially due to the presence of a single missense *Crls1* allele and the presence of CL. The $Crls1^{KO1}$ and $Crls1^{KO3}$ cells showed a more homogenous fragmented morphology, as both cell lines lacked CL. This indicates that CL is important for the reticular morphology of mitochondria. To validate that the reduction in CL caused the fragmented morphology, wild-type *Crls1* was introduced into $Crls1^{WT}$ and $Crls1^{KO3}$ cells. $Crls1^{KO3}$ regained the interconnected, tubular morphology observed in $Crls1^{WT}$ cells upon expression of wild-type *Crls1* but no changes were observed in the mock-transfected cells (Fig. 2C,D). Interestingly, $Crls1^{WT}$ transfected with WT *Crls1* demonstrated a minor increase in elongated tubular structures present in comparison to mock-transfected cells, indicating that CRLS1 overexpression can further increase fusion rates in wild-type cells (Fig. 2C,D).

Knockout of the fission regulating protein DRP1 (also known as DNM1L) had a minor effect on the mitochondrial morphology of the $Crls1^{KO3}$ cells compared to knockouts of the control, non-mitochondrial related protein EMX1 (Fig. 2E,F; Fig. S2B,C). $Crls1^{WT}$ *Drp1* KO cells showed a minor increase in mitochondrial network density and extension of the tubular network, with multiple cells containing regions of very dense mitochondrial regions that had a tangled appearance (Fig. 2E,F), consistent with previous findings (Otera et al., 2016). Together, these data indicate that impaired fusion is the main cause of the fragmented morphology of the knockout cells and impairing fission cannot adequately rescue this defect.

CL levels can affect the rate of mitochondrial protein synthesis and function

We measured *de novo* mitochondrial protein synthesis to determine whether it was affected by CL loss and disruption of the mitochondrial reticular network. Translation rates for all 13 mitochondrially encoded proteins were reduced in the three mutant cell lines compared to $Crls1^{WT}$ cells (Fig. 3A; Fig. S3A); however, $Crls1^{KO3}$ showed the least severe reduction despite

Journal of Cell Science (2020) 133, jcs240374. doi:10.1242/jcs.240374

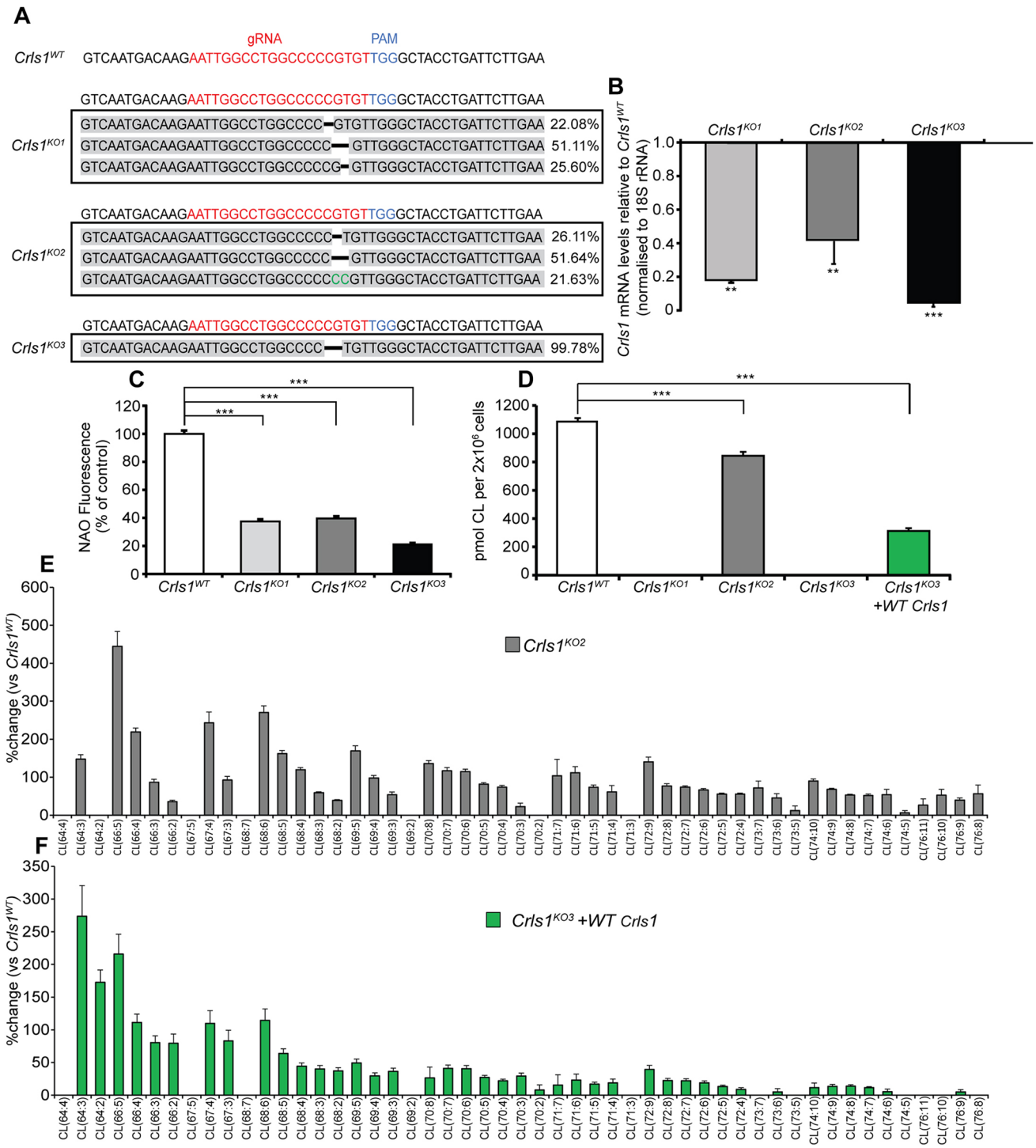

Fig. 1. Progressive loss of *Crls1* expression causes mitochondrial fragmentation. (A) Nextera sequencing of NIH-3T3 cell lines detailing edited alleles in the *Crls1*^{KO1}, *Crls1*^{KO2} and *Crls1*^{KO3} cell lines. Red text represents the guide RNA sequence, the protospacer adjacent motif (PAM) in blue, and green text represents inserted bases. (B) Levels of *Crls1* mRNA were determined in isolated total RNA from control (*Crls1*^{WT}), *Crls1*^{KO1}, *Crls1*^{KO2} and *Crls1*^{KO3} cell lines by qRT-PCR. Data are normalised to 18S rRNA levels and shown as mean±s.d. (n=6). (C) CL level was quantified in all cell lines using NAO (mean±s.d., n=6). (D) CL content was measured in 2×10^6 cells from control (*Crls1*^{WT}), *Crls1*^{KO1}, *Crls1*^{KO2}, and *Crls1*^{KO3} cell lines (mean±s.d.; n=5) by mass spectrometry. (E,F) The CL profile was determined from 2×10^6 cells for (E) *Crls1*^{KO2} cells and (F) *Crls1*^{KO3} cells transfected with wild-type CRLS1. Data are shown as mean±s.d. percentage change compared to *Crls1*^{WT} for each CL species. **P<0.01, ***P<0.001 (Student's t-test).

lacking CL. The steady state levels of the mitochondrially encoded subunits that make up the oxidative phosphorylation (OXPHOS) system, COXI, COXII and COXIII were decreased in *Crls1*^{KO3} cells, only COXI and COXII were decreased in *Crls1*^{KO1}, and none of these were significantly changed in the *Crls1*^{KO2} cells, consistent with the degree of loss of CL and CRLS1. Nuclear-encoded OXPHOS subunits were differentially affected in all cell lines; *Crls1*^{KO1} cells had an increase in complex V subunit ATP5A but

Journal of Cell Science (2020) 133, jcs240374. doi:10.1242/jcs.240374

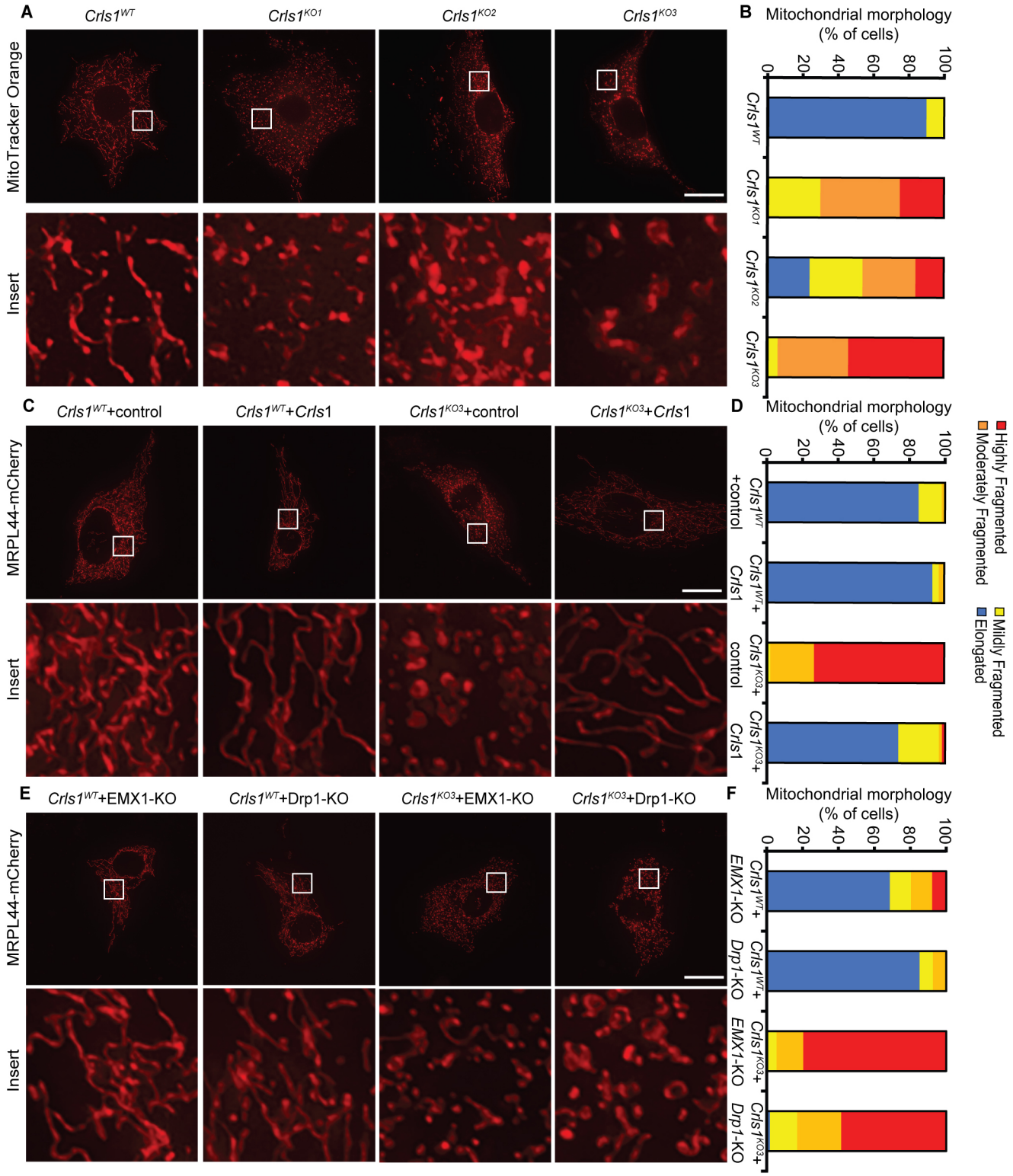

Fig. 2. Loss of CL causes impaired mitochondrial fusion. (A) Representative images of mitochondrial morphology in *Crls1*^{WT}, *Crls1*^{KO1}, *Crls1*^{KO2} and *Crls1*^{KO3} cell lines using MitoTracker Orange and visualised by fluorescence microscopy. (C,E) Representative images of mitochondrial morphology in *Crls1*^{WT} and *Crls1*^{KO3} (n>50) cell lines transfected with: control or Crls1 expressing plasmids (C), or EMX1 or Drp1 CRISPR knockout plasmids (E). Scale bars: 10 µm. (B,D,F) Morphology was visualised by means of the fluorescence of co-transfected protein MRPL44–mCherry. Qualitative scoring of mitochondrial morphology (n>50) for all cells. Details of morphology classifications are described in the Materials and Methods.

decrease in complex I subunit NDUFB8, *Crls1*^{KO2} showed a decrease in both subunits, and *Crls1*^{KO3} showed an increase in ATP5A compared to *Crls1*^{WT} cells (Fig. 3B; Fig. S3B). The complex II subunit, SDHA, was increased in *Crls1*^{KO3} cells and SDHB was increased in *Crls1*^{KO1} cells, which have the most reduced CL levels and most severe reticular network abnormalities.

Journal of Cell Science (2020) 133, jcs240374. doi:10.1242/jcs.240374

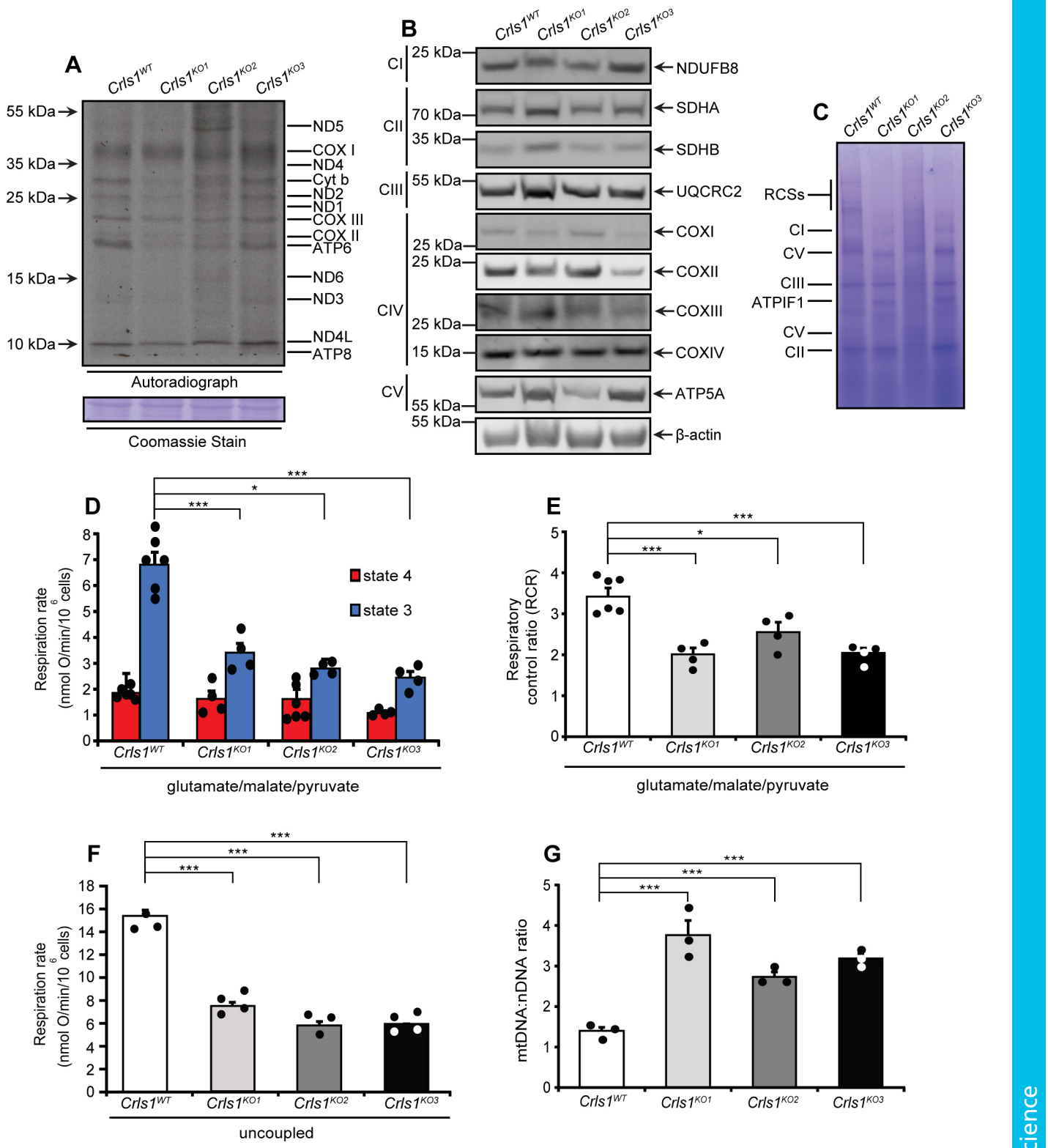

Fig. 3. CL supports mitochondrial protein synthesis and function. (A) *De novo* mitochondrial protein synthesis was measured in control (*Crls1*^{WT}), *Crls1*^{KO1}, *Crls1*^{KO2} and *Crls1*^{KO3} cell lines using ^{35}S-labelled methionine and cysteine. 20 µg of each cell lysate was separated by 12.5% SDS-PAGE and visualised by autoradiography. Equal loading was confirmed by Coomassie staining. (B) SDS-PAGE and immunoblotting for oxidative phosphorylation (OXPHOS) subunits was carried out using 25 µg of isolated mitochondrial lysates from control (*Crls1*^{WT}), *Crls1*^{KO1}, *Crls1*^{KO2} and *Crls1*^{KO3} cells. β-actin was used as a loading control. (C) Isolated mitochondria (80 µg) from control (*Crls1*^{WT}), *Crls1*^{KO1}, *Crls1*^{KO2} and *Crls1*^{KO3} cell lines were resolved by BN-PAGE and Coomassie stained. (D) Non-phosphorylated (state 4) and phosphorylated (state 3) respiration was measured in digitonin-permeabilised control (*Crls1*^{WT}), *Crls1*^{KO1}, *Crls1*^{KO2} and *Crls1*^{KO3} cells in the presence of glutamate/malate/pyruvate (n=6). (E) Respiratory control ratios were determined for glutamate/malate/pyruvate stimulated cells (n=6). (F) Maximal respiratory capacity was measured in the presence of FCCP in control (*Crls1*^{WT}), *Crls1*^{KO1}, *Crls1*^{KO2} and *Crls1*^{KO3} cells (n=4–6). (G) Mitochondrial DNA copy number was measured by means of qPCR for control (*Crls1*^{WT}), *Crls1*^{KO1}, *Crls1*^{KO2} and *Crls1*^{KO3} cells, and normalised to levels of *B2m*. Data are shown as mean±s.d. (n=3). *P<0.05, ***P<0.001 (Student's t-test).

Journal of Cell Science (2020) 133, jcs240374. doi:10.1242/jcs.240374

This increase is likely a compensatory response to reduced mitochondrial protein levels, as increased complex II activity and expression has been previously observed in diseases caused by OXPHOS defects (Duff et al., 2015; Pfleger et al., 2015).

CL loss altered the levels of native OXPHOS complexes and RCSs, composed of complexes I, III and IV, in all mutant cell lines, determined by Blue Native gel electrophoresis (Fig. 3C). The individual complexes were decreased in the *Crls1*^{KO1} and *Crls1*^{KO2} cells, while there were minor increases of these individual complexes in the *Crls1*^{KO3} cells. Additionally, all knockout cell lines displayed dramatic reduction in RCS levels, with *Crls1*^{KO1} and *Crls1*^{KO3} displaying negligible RCSs. The ATP inhibition factor 1 (ATPIF1) was released from complex V in the *Crls1*^{KO1} and *Crls1*^{KO3} cells, indicating a breakdown of higher order forms of complex V; this is a common response to OXPHOS defects in an effort for cells to prevent ATP hydrolysis and conserve energy (Mourier et al., 2014).

To examine the effects of CL loss on mitochondrial function, we measured oxygen consumption under phosphorylating and non-phosphorylating conditions in the presence of both glutamate, malate and pyruvate (GMP), and succinate and rotenone (Fig. 3D; Fig. S4A). GMP respiration was significantly reduced in all cell lines, but respiration on succinate in the presence of rotenone was unchanged. Similarly, respiratory control ratios (RCRs) were significantly decreased in the mutant cell lines under GMP stimulation (Fig. 3E), indicating an uncoupling of the electron transport chain (ETC) and ATP synthesis, but were unchanged in the presence of succinate (Fig. S4B). Maximal respiratory capacity was measured in the presence of FCCP and showed a significant decrease for all three cell lines (Fig. 3F). Taken together, these data indicate reduced OXPHOS function accompanied by an uncoupling of the ETC and ATP synthesis. The significant reduction in superoxide production measured by DHE fluorescence is consistent with reduced OXPHOS activity and the change in the CL profile (Fig. S4C).

Next, we investigated the effects of CL loss on mitochondrial DNA and gene expression. The mtDNA copy number was significantly increased in all three cell lines in response to compromised OXPHOS function, similar to previous observations in CL-deficiency condition Barth syndrome (Gonzalvez et al., 2013) (Fig. 3G). However, the steady levels of mtRNAs were unaffected in all knockout cell lines, indicating that the loss of CL does not affect the stability of mtRNAs (Fig. S4D).

Loss of CL causes compensatory increases in ER-related genes

We carried out RNA sequencing (RNA-seq) to understand the compensatory mechanisms responsible for the changes in OXPHOS complex formation and function when CL is lost or reduced (Fig. 4; Figs S5 and S6). Principal component analysis (PCA) of the gene expression matrix showed that the variance explained by the first principal component is consistent with the severity of the phenotype. The *Crls1*^{KO1} and *Crls1*^{KO3} cells occupied the top right quadrant, indicating that changes in gene expression in these cell lines correlated with severity of the mitochondrial network fragmentation (Fig. 4A). We analysed gene expression changes of CL biosynthesis enzymes that are localised to mitochondria and the endoplasmic reticulum (ER), and found that multiple genes, including *Gpat4*, *Agpat3*, *Agpat5*, *Lclat1* and *Taz*, showed similar changes across all cell lines, suggesting a common response to the loss of CL (Fig. 4B). However, the expression of the *Ptpmt1* mRNA, encoding the enzyme that catalyses the formation of the direct CL precursor PG, was increased only in the *Crls1*^{KO3} cells. An increase in the expression of *Gpat3*, encoding an ER protein, was observed in the *Crls1*^{KO1} and *Crls1*^{KO3} cells in contrast to *Gpam*, encoding a mitochondrial protein, which catalyses an identical reaction, which was only increased in the *Crls1*^{KO2} cells. This is consistent with the more-severe fragmentation of the mitochondrial network observed in these cells, and suggests an ER-specific response is induced as a consequence (Fig. 4B). In contrast, the residual CL synthase activity present in *Crls1*^{KO2} cells prevents complete fragmentation of the mitochondrial network and precludes activation of the ER stress response. The expression of the CL-modifying enzyme genes *Taz*, *Hadha* and *Hadhb* was increased and the expression of *Lclat8* was reduced in the *Crls1*^{KO2} cells, whereas the expression of only *Taz* and *Lclat8* was changed in the *Crls1*^{KO1} and *Crls1*^{KO3} cells. These expression changes are consistent with the higher levels of unsaturated acyl chain-containing CL precursor species identified in the lipid profiles of the *Crls1*^{KO2} cells compared to *Crls1*^{WT} cells, and could be a mitochondrially driven compensatory mechanism that is activated to overcome reduction in CL levels (Fig. 4B). The levels of the ER-stress factor mRNA *Ddit3*, along with two of its key targets *Trib3* and *Gadd34*, were significantly increased in the *Crls1*^{KO1} and *Crls1*^{KO3} cells indicating that a strong ER stress response is elicited in the absence of CL, where greater expression of these factors was found in the most severely fragmented mitochondrial network of the *Crls1*^{KO3} cells (Fig. 4C). In the *Crls1*^{KO2} cells, there was significantly elevated expression in *Ddit3* and *Gadd34*, but the least of all three cell lines, and a decrease in *Trib3*, consistent with there only being a reduction in CL levels and moderate fragmentation of the mitochondrial network. Taken together, these data indicate that the ER-stress response is involved in compensating for reduced mitochondrial function and altered mitochondrial morphology.

Expression of the transcription factors *Atf4* and *Atf5* was significantly increased in the *Crls1*^{KO3} cells, with a smaller increase only in *Atf5* in the *Crls1*^{KO1} cells, while there was a significant decrease in *Atf4* without any change to *Atf5* in the *Crls1*^{KO2} cells (Fig. 4C). Consistent with upregulation of *Atf4* and *Atf5* expression, *Crls1*^{KO3} cells showed the greatest changes in the expression of multiple mRNAs involved in mitochondrial biogenesis and translation (Fig. 4C; Fig. S5A). Additionally, ubiquinone biosynthesis and protease mRNAs were the most upregulated in *Crls1*^{KO3} cells, suggesting that higher protein turnover accompanies these compensatory responses (Fig. 4C; Fig. S6B). Several pathways related to nucleotide, cholesterol and carbon one metabolism were altered in the *Crls1*^{KO1} and *Crls1*^{KO2} cells, but only cholesterol biosynthesis was affected in the *Crls1*^{KO3} cells (Fig. 4D; Fig. S6). These changes suggest that a transcriptional stress response is elicited by the decrease and loss of CL in the *Crls1*^{KO1} and *Crls1*^{KO2} cells, whereas cholesterol biosynthesis is the major pathway that is affected in the absence of CL in all three cell lines with mutated *Crls1*. These findings illustrate that there are cell-wide compensatory mechanisms triggered by the loss of CL that can involve a multifaceted response from transcription factors that regulate mitochondrial and ER enzymes to compensate for changes in mitochondrial morphology and function.

CL is required for the stability of mitoribosomes

To investigate how mitoribosomes are affected by these compensatory responses, we examined whether the changes in CL levels affected the stability of mitoribosome proteins by immunoblotting. We found that the small subunit proteins

Journal of Cell Science (2020) 133, jcs240374. doi:10.1242/jcs.240374

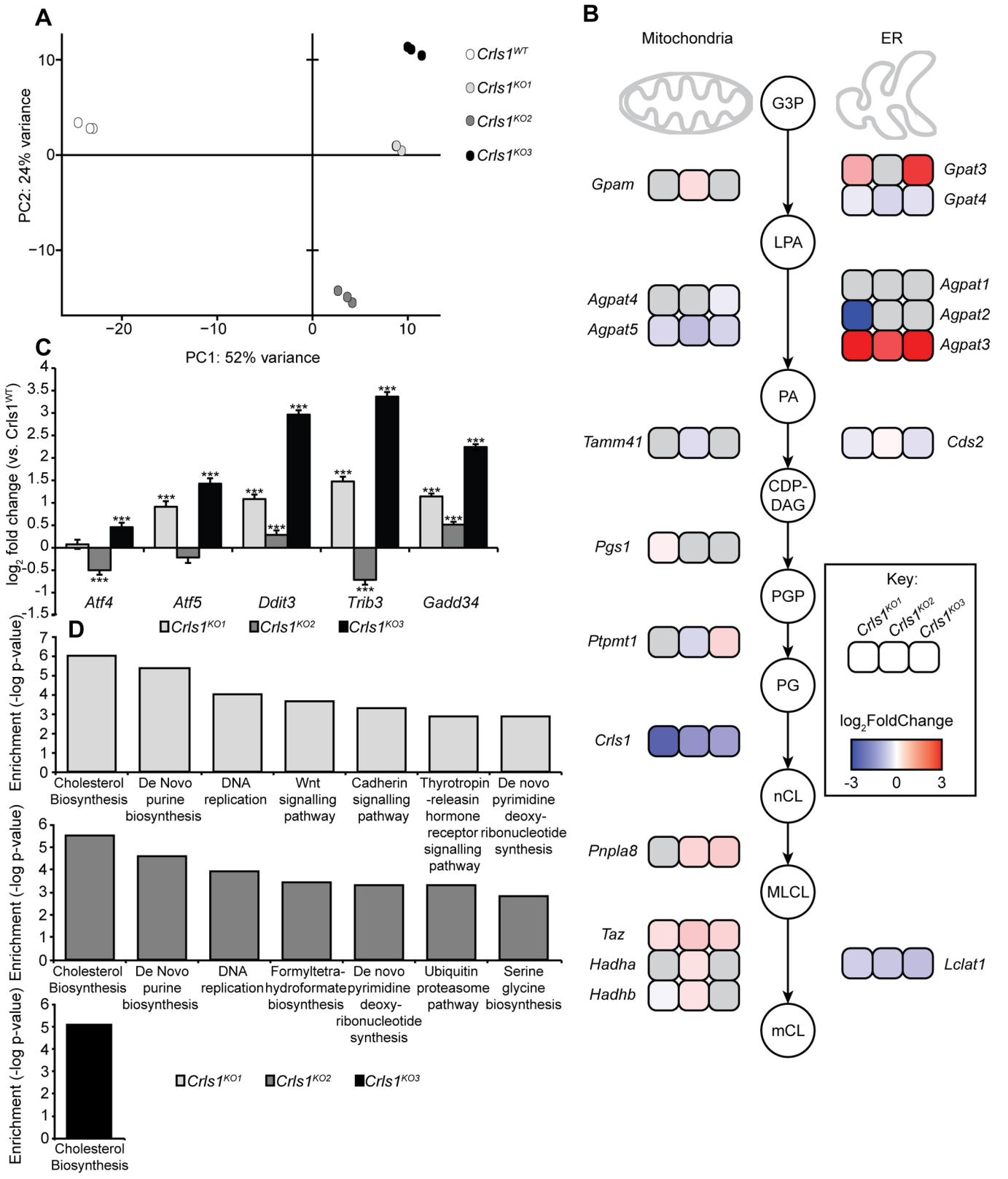

Fig. 4. Loss of CL causes compensatory changes in gene expression. (A) Principal component analysis of the variance-stabilised gene expression matrix in control (*Crls1*^{WT}) and *Crls1*^{KO1}, *Crls1*^{KO2} and *Crls1*^{KO3} cell lines (n=3 of each genotype). (B) Differential expression of CL biosynthesis enzymes comparing $\log_2$ fold changes between control (*Crls1*^{WT}) and *Crls1*^{KO1}, *Crls1*^{KO2} and *Crls1*^{KO3} cell lines (n=3 of each genotype). Non-significant changes are shown in grey. (C) Differential expression of *Atf4* and *Atf5*, and ER transcription factors between control (*Crls1*^{WT}) and *Crls1*^{KO1}, *Crls1*^{KO2} and *Crls1*^{KO3} cell lines (n=3 of each genotype). Results are mean±s.e.m. ***P<0.001 (Wald test). (D) Loss of CL causes transcriptional changes in genes associated with both nuclear and mitochondrial function. Gene ontology summary of the enriched processes that are uniquely altered in the *Crls1*^{KO1}, *Crls1*^{KO2} and *Crls1*^{KO3} cells compared to control (*Crls1*^{WT}) cells.

Journal of Cell Science (2020) 133, jcs240374. doi:10.1242/jcs.240374

MRPS34 and MRPS35 and large subunit proteins MRPL12 and MRPL44 were reduced in the *Crls1*^{KO1} and *Crls1*^{KO2} cells (Fig. 5A; Fig. S3C). In contrast, all of these ribosomal proteins were either significantly increased or not changed in the *Crls1*^{KO3} cells compared to control cells. Interestingly, the levels of MRPL45 were only increased in the *Crls1*^{KO1} cells compared to *Crls1*^{WT} (Fig. 5A; Fig. S3C).

Next, we investigated how changes in CL levels could impact mitoribosome assembly by resolving mitochondrial lysates on 10–30% sucrose gradients. The assembly of the mature 55S mitoribosome was reduced in the *Crls1*^{KO1} and *Crls1*^{KO2} cells, with an increased accumulation of the 28S small and 39S large subunits compared to the control cells (Fig. 5B). The assembly of the mature mitoribosome was less affected in the *Crls1*^{KO3} cells, where there was also a large increased accumulation of the individual 28S and 39S subunits. This suggests that the increase in ribosomal subunit proteins in *Crls1*^{KO3} cells compared to *Crls1*^{KO1} and *Crls1*^{KO2} cells can partially rescue mature mitoribosome formation by virtue of increased 28S and 39S subunit formation.

We investigated the distribution of mitoribosomes using confocal live-cell fluorescence microscopy by tagging the large ribosomal subunit protein MRPL12 with mCherry at the C-terminus and co-staining for mitochondria using MitoTracker Green. *Crls1*^{WT} cells showed a homogenous distribution of the mitoribosome throughout the mitochondrial network (Fig. 5C). Reduction or loss of CRLS1 in the three cell lines led to a heterogenous distribution of mitoribosomes that were primarily localised in punctate granule structures (Fig. 5C). Next, we investigated the association of the mitoribosome with CL at the mitochondrial membranes by examining the location of large ribosomal subunit protein MRPL45, which is thought to dock the mitoribosome to the inner membrane with CL. Initially, we tagged MRPL45 at its C-terminus with mCherry, which resulted in an inability of this protein to properly fold and caused overall mitoribosome destabilisation. Therefore, we used large ribosomal subunit protein MRPL44, which is closely associated with MRPL45 and also present at the membrane (Greber et al., 2014), to investigate whether the ribosome colocalises with CL. We used confocal live-cell fluorescent microscopy to visualise colocalisation of the mitochondrial ribosome with CL by tagging mCherry to the C-terminus of MRPL44 and using the green fluorescent CL-binding compound NAO (Fig. 5D). The loss of a homogenous distribution of the mitoribosome was shown to be accompanied by a loss of discrete CL-containing tubular structures in all knockout cell lines, which was most notable in the *Crls1*^{KO3} cells, which have almost no discernible CL tubular structures. Interestingly, *Crls1*^{KO2} cells, which have a mix of tubular and granular structures, show colocalisation of the mitoribosome and CL only in the tubular structures and not the granular structures, indicating that CL may have a role in coordinating mitoribosome attachment and distribution throughout the mitochondrial network (Fig. 5D).

OXA1 colocalisation with the mitoribosome at the inner membrane is mediated by CL

The irregular distribution of mitoribosomes resulting from diminished CL levels led us to investigate whether the insertase protein OXA1, hypothesised to interact with the N-terminal tail of MRPL45 to facilitate mitoribosome docking and translation initiation (Kummer et al., 2018), might have this potential association altered in the absence of CL. We used MRPL44 tagged with GFP at its C-terminus and OXA1 tagged with mCherry at its C-terminus to show their colocalisation in *Crls1*^{WT} cells using super resolution microscopy (Fig. 6A). This colocalisation was significantly diminished in the *Crls1*^{KO3} cells (Fig. 6B), indicating that CL is required for optimal mitoribosome docking and association with OXA1. Next, we truncated amino acids 332–433, predicted to act as the mitoribosome-binding region of OXA1 (Haque et al., 2010a,b), and tagged this truncated OXA1 (OXA1Δ332) protein with mCherry at its C-terminus. Super resolution microscopy revealed that the OXA1Δ332 truncation reduces the colocalisation of the mitoribosome with OXA1 in *Crls1*^{WT} cells, indicating that this region mediates the association of OXA1 with the mitoribosome at the inner membrane (Fig. 6C). Interestingly, steady state levels of OXA1 were increased in all knockout cell lines (Fig. 6D; Fig. S3D), indicating that increases in OXA1 may be an attempt to compensate for the impaired association of OXA1 with the mitoribosome.

Next, we investigated whether the mitoribosome associates with OXA1 and docks on the inner membrane during translation initiation and active translation. We examined the colocalisation of OXA1 and MRPL44 in *Crls1*^{WT} cells in the presence and absence of the mitochondrial translational inhibitor chloramphenicol. Vehicle-treated cells maintained the colocalisation of OXA1 and the mitoribosome; however, when translation was inhibited in the presence of chloramphenicol, this colocalisation was highly disturbed (Fig. 6E,F), suggesting that this interaction may occur during active translation.

To further examine the interaction of the mitoribosome and OXA1, *Crls1*^{WT} and *Crls1*^{KO3} cells were transfected with GFP-tagged MRPL12 and either mCherry-tagged OXA1 or an unfused mCherry tag. Immunoprecipitation of the mCherry tag, following crosslinking, was examined by immunoblotting to determine whether MRPL12–GFP associated with OXA1 (Fig. 6G). In *Crls1*^{WT} OXA1–mCherry-transfected cells, both MRPL12–GFP and untagged OXA1 were identified in the elution fraction, but neither were present in the control, unfused mCherry-tagged, elution fraction. MRPL12–GFP was not identified in the elution fraction from the *Crls1*^{KO3} cells, but untagged OXA1 was present. This indicates that a homo-oligomeric OXA1 complex interacts with the mitoribosome and that this interaction is perturbed by the loss of CL.

To independently validate these associations between the mitoribosome and OXA1, bimolecular fluorescent complementation (BiFC) was used, and the Venus fluorescent signal was measured by fluorescence-activated cell sorting (FACS). The Venus fluorescent protein was fragmented into two, non-fluorescent fragments (VN and VC) and each fragment was attached to MRPL44 and OXA1. Direct protein interaction, in this case between MRPL44 and OXA1, would bring the two Venus fragments together restoring the fluorescence of the Venus protein (Morell et al., 2008; Wang and Carnegie, 2013). Expression of OXA1–VN and MRPL44–VC fragments resulted in a fluorescent signal, validating their interaction in the *Crls1*^{WT} cells (Fig. 7A,B; Figs S7, 8A). Comparatively, the interaction between OXA1Δ332–VN and MRPL44–VC produced both a significantly reduced number of positive cells and decreased average fluorescence intensity of these positive cells, indicating reduced interaction (Fig. 7A,B; Figs S7, 8A). Additionally, cells treated with chloramphenicol had a significantly reduced number of positive cells and reduced average fluorescence intensity compared to cells treated with a vehicle control, suggesting that active translation facilitates the interaction between OXA1 and the mitoribosome (Fig. 7A,B; Figs S7, 8A). In the *Crls1*^{KO3} cells, the interaction between OXA1–VN and MRPL44–VC was also observed; however,

Journal of Cell Science (2020) 133, jcs240374. doi:10.1242/jcs.240374

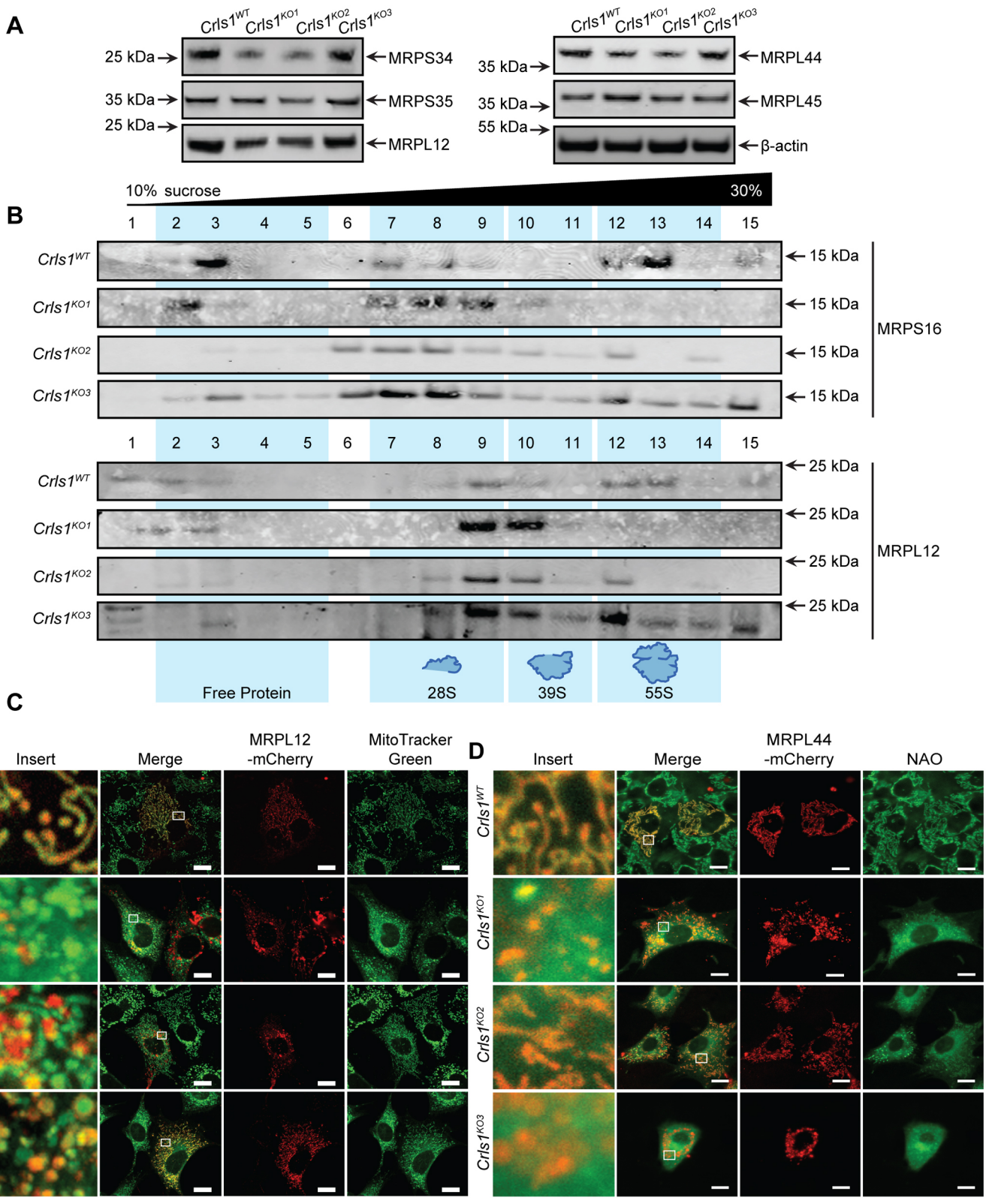

Fig. 5. CL is required for mitoribosome stability. (A) Isolated mitochondrial lysates (25 µg) from control (*Crls1*^{WT}), *Crls1*^{KO1}, *Crls1*^{KO2} and *Crls1*^{KO3} cells were resolved by SDS-PAGE and immunoblotted for mitoribosomal subunits. β-actin was used as a loading control. (B) Cell lysates from control (*Crls1*^{WT}), *Crls1*^{KO1}, *Crls1*^{KO2} and *Crls1*^{KO3} cells were resolved on a continuous 10–30% sucrose gradient to analyse the distribution of the small subunit, large subunit and monosomes. Mitochondrial ribosomal protein markers of the small (MRPS16) and large (MRPL12) subunits were detected by immunoblotting. (C) Mitoribosome distribution was examined by live-cell fluorescence microscopy in control (*Crls1*^{WT}), *Crls1*^{KO1}, *Crls1*^{KO2} and *Crls1*^{KO3} cells using MRPL12–mCherry and MitoTracker Green. (D) Mitoribosomal colocalisation with CL was examined by live-cell fluorescence microscopy in control (*Crls1*^{WT}), *Crls1*^{KO1}, *Crls1*^{KO2} and *Crls1*^{KO3} cells using MRPL44–mCherry and NAO. Data are representative of at least three independent biological replicates (n=6). Scale bars: 5 µm.

Journal of Cell Science (2020) 133, jcs240374. doi:10.1242/jcs.240374

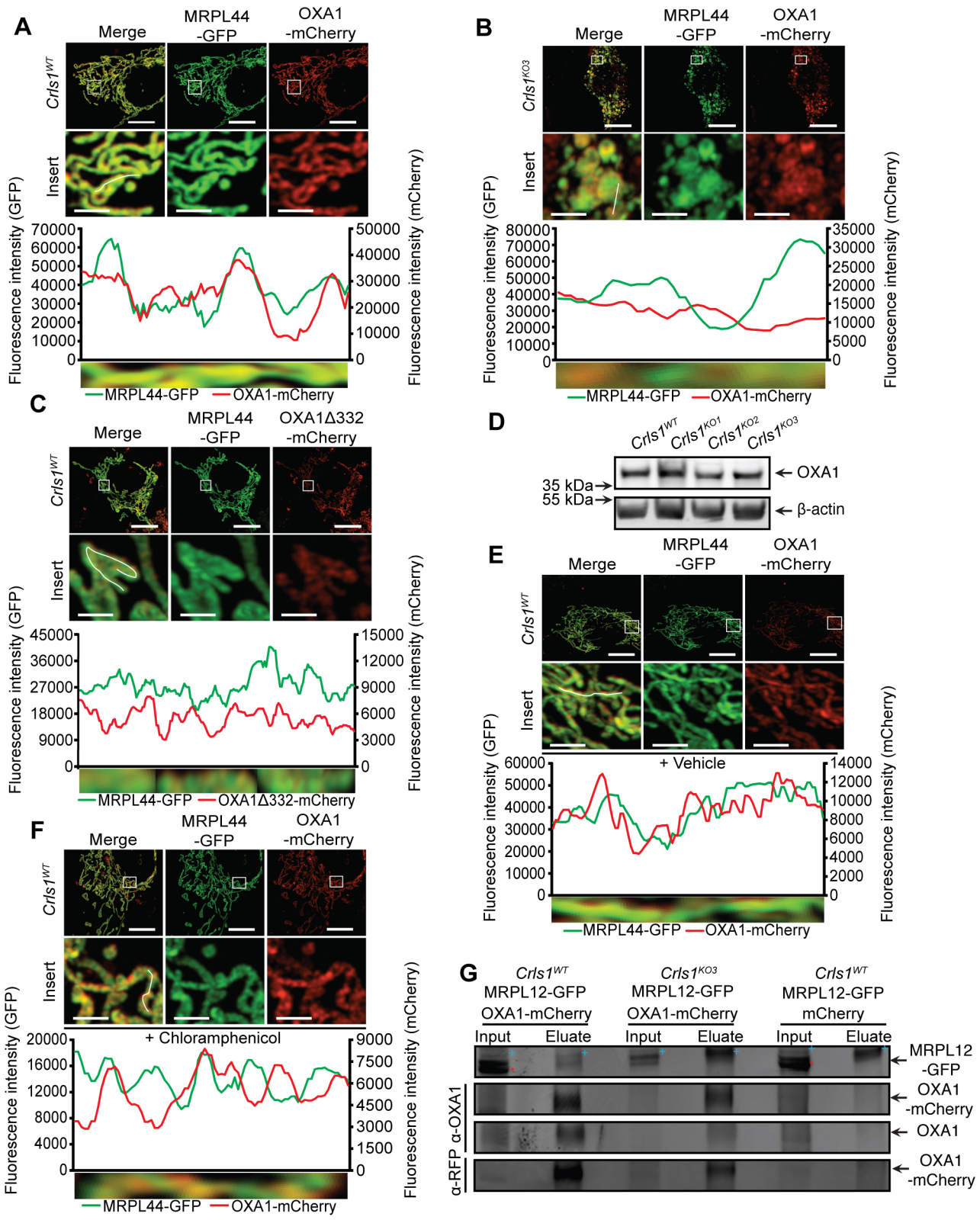

Fig. 6. CL mediates the interaction of the mitoribosome and OXA1. (A–C,E,F) Localisation of MRPL44–GFP and OXA1–mCherry in *Crls1*^{WT} (A) and *Crls1*^{KO3} (B) cells, and MRPL44–GFP with the truncation mutant OXA1Δ332–mCherry in *Crls1*^{WT} cells (C) was examined using super resolution fluorescence microscopy. Where indicated, *Crls1*^{WT} cells were treated with either vehicle (ethanol) (E) or chloramphenicol (F). Insets are taken from area encompassed by the white rectangle. White lines on insert images represent the area that was used for quantitation, which is also represented in the graph under the respective image. (D) SDS-PAGE and immunoblotting for OXA1 was carried out on 25 µg of isolated mitochondrial lysates from control (*Crls1*^{WT}), *Crls1*^{KO1}, *Crls1*^{KO2}, and *Crls1*^{KO3} cell lines. (G) Immunoprecipitation of mCherry from *Crls1*^{WT} or *Crls1*^{KO3} cells expressing GFP-tagged MRPL12 and either mCherry-tagged OXA1 or unfused mCherry, to act as a negative control, followed by immunoblotting of both input and elution samples. * denotes a low molecular mass non-specific band and '+' denotes a high molecular mass non-specific band. Data are representative of at least five independent biological replicates. Scale bars: 10 µm (main images); 2.5 µm (inset).

Journal of Cell Science (2020) 133, jcs240374. doi:10.1242/jcs.240374

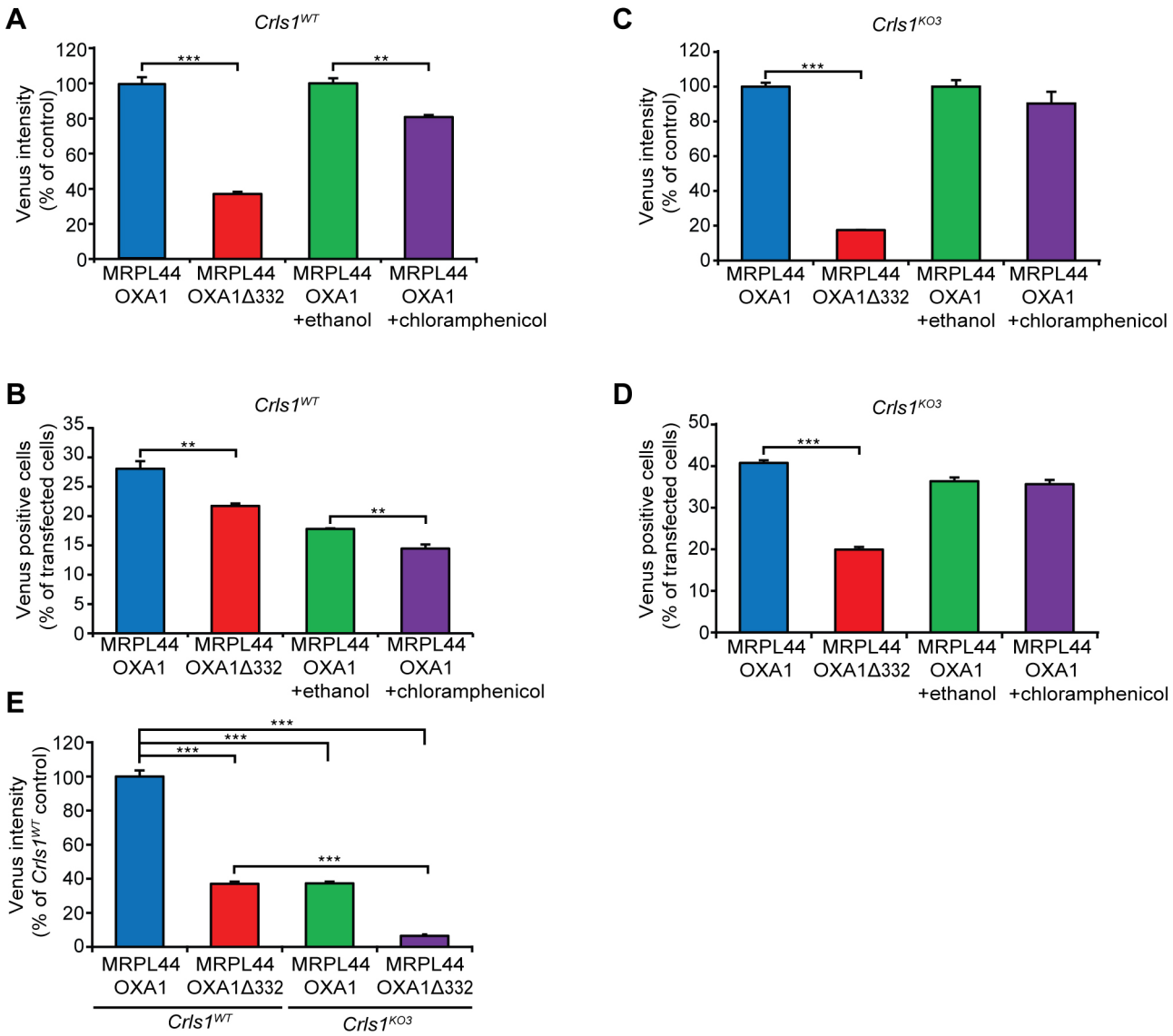

Fig. 7. Loss of CL alters the dynamics of the mitoribosome–OXA1 interaction. Intensities of Venus versus RFP in (A,B) *Crls1*^{WT} and (C,D) *Crls1*^{KO3} cells determined by FACS for all respective treatments (n=3). Average Venus intensities normalised to RFP intensity for (A) *Crls1*^{WT} and (C) *Crls1*^{KO3} cells. Data are shown as a percentage change compared to the respective control and percentage of transfected cells (RFP positive) that were Venus positive for (B) *Crls1*^{WT} and (D) *Crls1*^{KO3} cells. (E) Average Venus intensities normalised to RFP intensity comparing interactions between *Crls1*^{WT} and *Crls1*^{KO3} cells. Data are representative of three independent biological replicates and shown as mean±s.d. $^{**}P$<0.01, $^{***}P$<0.001 (Student's t-test).

the reduction of this interaction for OXA1Δ332–VN and MRPL44–VC transfected cells was greater than in the *Crls1*^{WT} cells (Fig. 7C,D; Figs S7, 8B). Interestingly, the fluorescence intensity was not affected with the chloramphenicol treatment in the *Crls1*^{KO3} cells, indicating the interaction between OXA1 and MRPL44 can be stochastic in the absence of CL and elongation of protein synthesis (Fig. 7C,D, Figs S7, 8B). Finally, we compared the OXA1–VN and MRPL44–VC interaction between the *Crls1*^{WT} and *Crls1*^{KO3} cells, and show that this interaction is reduced significantly in the absence of CL (Fig. 7E). The interaction between OXA1Δ332–VN and MRPL44–VC was further reduced in the *Crls1*^{KO3} cells compared to *Crls1*^{WT} cells (Fig. 7E). This indicates that both CL and the C-terminal end of OXA1 facilitate the association between the mitoribosome and OXA1.

These findings indicate that, during translation elongation, the mitoribosome forms a stable association with OXA1, mediated by CL, docking it at the inner membrane to facilitate membrane insertion of *de novo* translated OXPHOS subunits.

DISCUSSION

The mitochondrial protein synthesis machinery is intimately linked to OXPHOS complex biogenesis, structural dynamics and ATP production, which can respond to changes in energy requirements and diverse cellular conditions (Lee et al., 2018). Recently, evidence has emerged that the mitoribosome may interact with the inner mitochondrial membrane to facilitate insertion of the newly synthesised respiratory complex subunits directly into the membrane. Here, we generated a series of models of mitochondrial inner membrane dysfunction through the progressive loss of CRLS1, which reduced CL content in the inner membrane. We used these cells to investigate how changes in the inner membrane and CL can influence the protein synthesis machinery and translation. The three cell lines we developed have differentially altered CL levels and profiles. While *Crls1*^{KO1} and *Crls1*^{KO3} cells had negligible levels of CL, *Crls1*^{KO2} cells had a reduction in CL levels compared to *Crls1*^{WT} as well as an altered CL profile. The

Journal of Cell Science (2020) 133, jcs240374. doi:10.1242/jcs.240374

changes in the lipid profile of the *Crls1*^{KO2} cells showed that impaired CL biosynthesis leads to accumulation of shorter acyl chain length and more highly unsaturated CL precursors. This could be either because these species are kinetically favoured during biosynthesis or that these species are favoured by cells to maintain optimum function when CL levels are reduced. LCLAT1 has been shown to be responsible for the incorporation of long chain fatty acids like docosahexaenoic acid (DHA) (22:8) and decreased abundance of shorter chain CL species (Li et al., 2010). Therefore, LCLAT1 downregulation would contribute to the reduction in long acyl chain containing CL species, as we observed in the *Crls1*^{KO2} and *Crls1*^{KO3} rescue CL profiles. *Lclat1* suppression has been shown to confer resistance to stress, like reactive oxygen species (ROS) insult and metabolic stress from high fat diets in mice (Li et al., 2010; Song et al., 2019), and overexpression of *Lclat1* has been shown to cause dysfunction to mitochondrial fusion and OXPHOS function (Li et al., 2010, 2012). This indicates that the downregulation of LCLAT1 across all cell lines could be a compensatory mechanism to preserve cell survival when CL levels are low. Conversely, both TAZ, and the mitochondrial trifunctional proteins HADHA and HADHB, have been shown to incorporate linoleic acid (18:2) and mature CL to a give a more-unsaturated CL profile (Claypool and Koehler, 2012; Miklas et al., 2019; Soustek et al., 2010; Taylor and Hatch, 2009; Xu et al., 2006). Therefore, their upregulation may cause the increased levels of unsaturated species of shorter chain lengths as was found in the *Crls1*^{KO2} cells. Interestingly, studies on *Hadha* KO and *Hadha* compound heterozygote cardiomyocyte stem cells has revealed similar CL profiles to the *Crls1*^{KO2} and *Crls1*^{KO3} rescue cells, with shorter chain-containing CL species most heavily upregulated and larger species either unchanged or downregulated compared to controls (Miklas et al., 2019). The hypothesis that shorter CL species are preferentially incorporated when CL levels are low is supported by the CL profile of the *Crls1*^{KO3} rescue cells, where the shorter chain CL species were elevated after 72 h of rescue. It is possible that these shorter chain length species require the least cellular effort to produce and can be rapidly introduced to preserve cell function, and this could explain the restoration of mitochondrial morphology in our CL knockout cell line.

The progressive loss of CL resulted in fragmented mitochondrial morphology and uncoordinated mitochondrial translation. Uncoordinated translation caused decreased mitochondrial respiration and contributed to decreased superoxide production, indicating that CL is important for mitochondrial structure and respiratory function as previously observed (Dudek, 2017; Paradies et al., 2014). We have identified previously that impaired assembly of the large ribosomal subunit can affect the morphology of the mitochondrial cristae, linking gene expression to changes in mitochondrial dynamics (Kummer et al., 2018; Perks et al., 2017). Here, we show that changes in the membrane can affect mitochondrial translation, indicating that biogenesis within mitochondria is affected by inner mitochondrial membrane composition.

Mitochondrial OXPHOS biogenesis was affected by the loss of CL, as the formation of the RCSs was reduced. RCSs have been suggested to facilitate electron transport between the individual complexes and reduce the loss of electrons throughout the process (Dudkina et al., 2011; Genova and Lenaz, 2014), and their reduction affected the efficiency of ETC coupling in the CL-deficient cells. Reduction in supercomplex formation resulting in ETC uncoupling has been previously observed in Barth syndrome patient cells, which produce abnormal CL due to mutation of a phospholipid transacylase involved in CL remodelling in mitochondrial membranes (Gonzalvez et al., 2013). This reduction in mitochondrial OXPHOS function is a consequence of ETC uncoupling and reduced levels of OXPHOS RCSs that are not assembled properly in the absence of CL that is in turn required for their stability and assembly (Osman et al., 2011).

Mitoribosome subunits increased in abundance in *Crls1*^{KO3} cells, perhaps in an attempt to compensate for the impaired translation, in a similar manner to the increased expression of complex II that compensates for reduced ETC activity. Similar increases in ribosomal subunit expression have been observed in other models of mitochondrial dysfunction where mitoribosome formation was impaired. It is possible that this increase in subunit expression is an attempt to rescue impaired monosome formation (Cámara et al., 2011; Metodiev et al., 2014; Rackham et al., 2016). The increase in mitoribosomal protein expression resulted in increased formation of the individual subunits and consequently a minor increase in monosome formation in *Crls1*^{KO3} compared to the *Crls1*^{KO1} and *Crls1*^{KO2} cell lines. These increases were shown to be a part of a greater compensatory mechanism in *Crls1*^{KO3} cells, potentially orchestrated by increases in ATF4 and ATF5, which have been observed to increase in response to mitochondrial translation defects that likely contribute to the increased mtDNA levels previously (Ferreira et al., 2019). Similarly, an ER stress response driven by increased levels of *Ddit3* has been observed upon *Crls1* knockout in brown adipose tissue (Sustarsic et al., 2018). *Crls1*^{KO3} cells showed the most prominent changes in the expression of genes associated with mitochondrial biogenesis and translation out of the three cell lines, which is consistent with increases in *Atf4*, *Atf5* and *Ddit3* expression. As ATF4 and DDIT3 have been previously shown to work synergistically to modulate increased expression of genes involved in protein synthesis (Han et al., 2013), this multi-faceted response could explain how *Crls1*^{KO3} cells had the least severe reduction in translation. These responses illustrate a mechanism by which the cell can respond to an inability of the mitoribosome to properly associate with the inner membrane. Interestingly, *Crls1*^{KO2} cells display either minor or no significant changes in any of these transcription factors, indicating that their response to defects is an independent mechanism and driven through CL modification enzymes. While the response of the *Crls1*^{KO3} may partially rescue defects in translation, defects in the formation of RCSs, coupling of the ETC and heterogeneous mitoribosome distribution were not rescued. This demonstrates that while increasing the abundance of proteins and complexes produced can rescue translation rates, it is not enough to overcome the uncoordinated nature of the translation arising from fragmented inner membrane morphology and lack of CL or the formation of the RCSs. While the *Crls1*^{KO2} compensatory response could not rescue translation levels, morphology, ribosomal distribution, RCS formation and CL levels were the least affected, indicating that the presence of CL precursors can maintain some CL-related function. Our findings identify two separate compensatory mechanisms in cells where CL is reduced and lost. Reduction in CL levels causes changes in CL remodelling enzyme expression levels that lead to increased formation of more functionally favourable CL species, sufficient for mitochondrial function and structure. In the absence of CL, both ER and mitochondrial transcription factors coordinate a multifaceted response to increase the expression of proteins involved in mitochondrial gene expression in an attempt to overcome the loss of coordinated translation. The biochemical similarity between our knockout cells and cells from Barth syndrome patients (Gonzalvez et al., 2013) illustrates the potential use of CL

Journal of Cell Science (2020) 133, jcs240374. doi:10.1242/jcs.240374

knockout cells to understand how altering the dynamics of mitochondrial lipids and the gene expression machinery can impact human disease.

We show that CL levels are required for the homogeneous distribution of mitoribosomes throughout the cell. This is evident in the *Crls1*^{KO2} cells where CL is only reduced, but not entirely lost, resulting in a hybrid morphology containing both tubular and granular mitochondria. CL and the mitoribosomes colocalise and have a more organised distribution in the tubular structures but not in the granular structures. Structural studies have suggested that the C-terminal end of MRPL45 may anchor the mitoribosome in the membrane (Greber et al., 2014). Here, we showed that CL reduction affected the assembly of the mitoribosome and its association with OXA1, suggesting that CL stabilises this interaction at the membrane. The same kind of disruption was seen when OXA1 was replaced with the OXA1Δ332 mutant in *Crls1*^{WT} cells, which would remove the predicted mitoribosome-binding domain (Haque et al., 2010a,b), demonstrating that the mitoribosome interacts directly with OXA1 and CL facilitates this interaction. In addition, it is possible that CL has a role in maintaining an even distribution of mitoribosomes across the membrane, and that the lack of CL causes mitoribosomal distribution to become dysregulated.

The colocalisation of the mitoribosome and OXA1 may be a required step during the translation cycle since inhibiting translation disturbed the colocalisation of these proteins, and that this interaction is stabilised by CL. This establishes a model for mitochondrial translation involving the interaction of the mitoribosome and an OXA1 homo-oligomer. CL facilitates the association of the mitoribosome and OXA1 at the membrane, and a stable interaction is formed between the OXA1 homo-oligomer and the mitoribosome during translation. This allows for newly synthesised proteins to exit the ribosome and be directly inserted into the membrane, where they can assemble into RCSs (Fig. 8A). The coordinated biogenesis seen in *Crls1*^{WT} cells, where the mitoribosome and OXA1 are anchored at the inner membrane by CL, is distorted in the *Crls1*^{KO3} cells and may be a stochastic association. OXA1 and the mitoribosome may encounter each other during random movement of proteins through the membrane, ultimately resulting in a less stable interaction and uncoordinated translation. This may also explain the lack of RCSs in the three cell lines as the mitoribosomes require close proximity to respiratory complexes to facilitate their assembly with *de novo* produced mitochondrial polypeptides. The inability of CL to create a platform where the mitoribosome and OXA1 can stably interact may result in a more transient interaction between the two, which may be insufficient to synthesise and insert all components of the RCSs at one site in the membrane, resulting in respiratory complexes being synthesised individually in separate areas of the membrane and leading to an impaired coupling of electron transport between them. The increase in expression of the mitoribosomal subunits can partially rescue formation of the mature monosome but may not be able to overcome the inability of the mitoribosome to stably interact

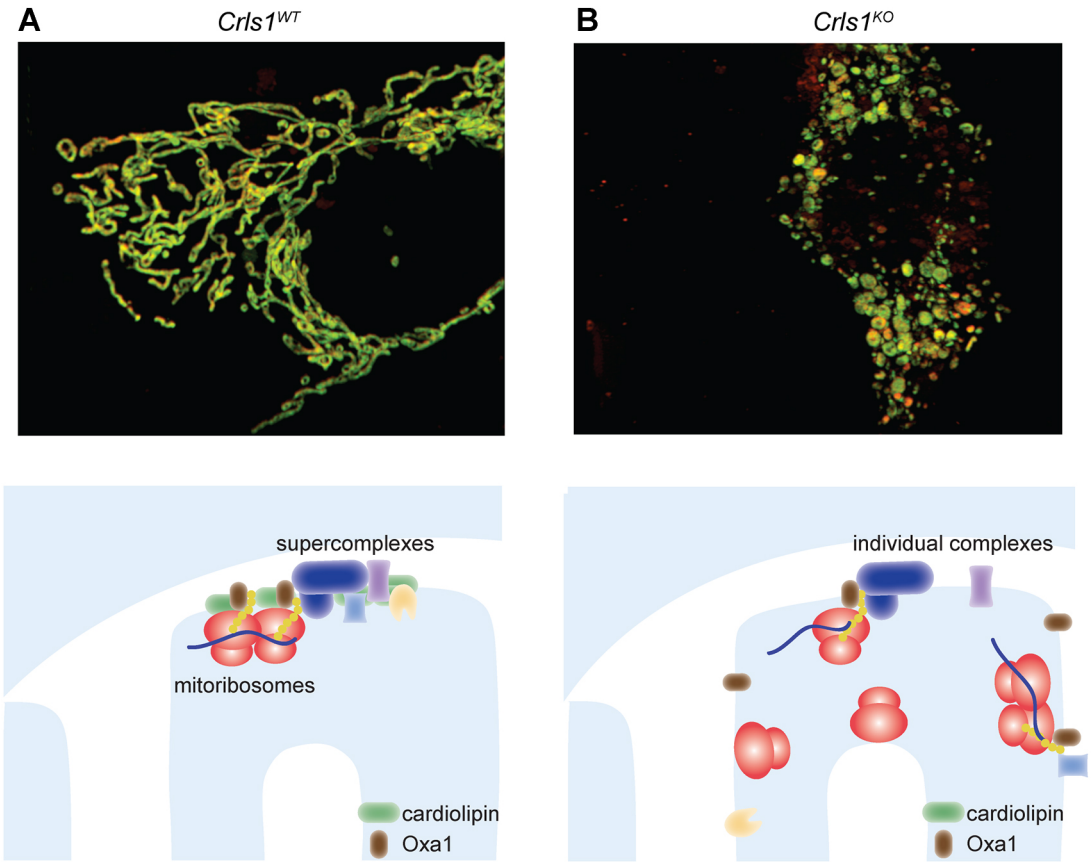

Fig. 8. Model of mitochondrial protein synthesis at the inner membrane. (A) When mitochondrial protein synthesis is initiated, CL mediates the association of the mitoribosome and OXA1 at the inner membrane. CL serves as a platform for the mitoribosome and OXA1 to interact, allowing for newly synthesised proteins to be inserted directly into the membrane. This stable interaction supports the assembly of the respiratory chain supercomplexes. (B) Loss of CL precludes the interaction of the mitoribosome with OXA1, which reduces the rate of protein synthesis in the *Crls1*^{KO} cell lines. Here, the mitoribosome and OXA1 have no stable platform to interact on so their association may be stochastic, and results in reduced supercomplex assembly.

Journal of Cell Science (2020) 133, jcs240374. doi:10.1242/jcs.240374

with OXA1, which ultimately cannot fully rescue protein synthesis, as seen in the *Crls1*^{KO3} cells (Fig. 8B).

Our work indicates that active translation takes place at the mitochondrial inner membrane and that this is advantageous to facilitate the assembly of the highly hydrophobic OXPHOS proteins within the inner membrane. This may be separated from the mitochondrial gene expression machinery by means of the mitochondrial granules where it is suggested that the mtRNAs are stabilised and regulated by RBPs and the beginning stages of mitoribosome assembly take place (Antonicka and Shoubridge, 2015; Bogenhagen et al., 2014; Jourdain et al., 2016). The unique structure and function of mitoribosomes reveal new mechanisms by which animals regulate the biogenesis of the OXPHOS system. It would be of great interest to identify the evolutionarily distinct and common mechanisms of translational control in other organelles and diverse species in the future.

MATERIALS AND METHODS

Cell culture

NIH-3T3 cells were cultured at 37°C in humidified 95% air/5% CO_2 in Dulbecco's modified Eagle's medium (DMEM; Gibco, Life Technologies) containing glucose (4.5 g/l), glutamine (2 mM), fetal bovine serum (FBS; 10%), penicillin (100 U/ml), streptomycin sulphate (100 µg/ml), sodium pyruvate (1 mM) and uridine (50 µg/ml). The cells were obtained from ATCC, authenticated by STR profiling and found to be free of mycoplasma.

Stable transfections and FACS

NIH-3T3 cells were seeded in six-well plates at 60% confluency, allowed to attach, and transfected with 1.5 µg of a pD1311-AD mammalian Cas9 expression vector (ATUM) encoding a *Crls1*-targeting gRNA using FuGENE HD (Promega) in Opti-MEM (Invitrogen, Thermofisher). For establishing stably transfected colonies, single-cell sorting was performed on the transfected cell population 72 h post transfection, where individual cells were sorted into 96-well plates based on GFP fluorescence signal using a FACSAria II (BD Biosciences) in PBS plus 2% (v/v) FBS. Loss of *Crls1* alleles was confirmed by both Sanger sequencing and Nextera sequencing of PCR-amplified gDNA performed by the Australian Genomic Research Facility (AGRF). All primer and guide sequences are described in Table S1.

Transient transfections

NIH-3T3 cells were seeded at 60% confluency, allowed to attach and transfected with 158 ng/cm^2 of plasmid DNA for single-plasmid transfection and transfected with 263 ng/cm^2 for double- and triple-plasmid transfections. Single-plasmid transfections were performed with FuGENE HD in Opti-MEM. Double- and triple-plasmid transfections were performed using a 1:1 ratio of FuGENE HD and Lipofectamine LTX (Invitrogen) in Opti-MEM. Experiments were performed 72 h post transfection.

Cell lysate isolation

NIH-3T3 cells were trypsinised, and resuspended in a lysis solution containing 150 mM NaCl, 0.1% Triton X-100 and 50 mM Tris-HCl (pH 8) for 30 min at 4°C. Then, cells were centrifuged at 21,000 ***g*** for 15 min at 4°C to clarify lysates. Protein concentration was determined using a BCA assay.

Mitochondrial isolation

Mitochondria were isolated from NIH-3T3 cells by differential centrifugation using a buffer containing 250 mM sucrose, 1 mM EGTA, and 5 mM Tris-HCl (pH 7.4) as previously described (Rackham et al., 2009). Protein concentration was determined using a BCA assay.

Dihydroethidium measurements

NIH-3T3 cells were seeded in black 96-well plates and allowed to attach overnight. Cells were stained with 10 µM dihydroethidium (DHE) (Molecular Probes, Thermofisher) in FBS-free DMEM and incubated for 45 min at 37°C. Cells were washed in PBS and 0.1% (v/v) Triton X-100 in PBS was added to cells. Fluorescence readings were taken at 590 nm using a CLARIOstar. Fluorescence values were expressed as a percentage of the average wild-type cell fluorescence intensity.

Northern blotting

5 µg of isolated RNA from NIH-3T3 cells was separated on 1.2% agarose formaldehyde gels, transferred to 0.45 µm Hybond-N$^+$ nitrocellulose membranes (GE Lifesciences), and hybridised with biotinylated oligonucleotide probes for specific mitochondrial mRNA, tRNA and rRNA sequences (Rackham et al., 2009). Hybridisation was performed in 5× saline sodium citrate (SSC), 20 mM Na_2HPO_4, 7% SDS, and 100 µg/ml heparin at 50°C overnight. Probes were detected using streptavidin-linked infrared-labelled antibodies diluted 1:2000 in 3× SSC, 5% SDS and 25 mM Na_2HPO_4 (pH 7.5) using an Odyssey infrared imaging system (Li-COR Biosciences).

RNA isolation and qRT-PCR

RNA was isolated from NIH-3T3 cells using a miRNeasy MiniKit (Qiagen), incorporating an on-column RNase-free DNA digestion, according to the manufacturer's instructions. cDNA was prepared using a Quantitect Reverse Transcription Kit (Qiagen) and used as a PCR template. Amplification was conducted in a Corbett Rotorgene 6000 using SensiMix SYBR mix (Bioline). All values were normalised to 18S rRNA. All primers used are detailed in Table S1.

NAO staining for CL quantification

NIH-3T3 cells were seeded in black 96-well plates and allowed to attach overnight. Cells were stained with 5 µM Nonyl Acridine Orange (NAO) (Molecular Probes, Thermo Fisher Scientific) in FBS-free DMEM and incubated for 30 min at 37°C. Cells were washed in PBS and fluorescence readings were taken in PBS at 530 nm using a CLARIOstar (BMG Biotech). Fluorescence values were expressed as a percentage of the average wild-type cell fluorescence intensity and normalised to the fluorescence of wild-type cells.

Lipid extraction

Samples (2×10^6 cells each) were lyophilised then homogenised by adding 50–100 mg zirconium oxide beads (0.15 mm; Next Advance), 200 µl ice-cold 60% (v/v) methanol in water, 50 µl of a customised internal lipid standard mix in chloroform [including CL(14:0/14:0/14:0/14:0) at a concentration of 15.7 µM] and subsequently blending using a bullet blender (Next Advance) for three cycles of each 30 s at speed 8. Samples were frozen on dry ice in between cycles for 30 s. Then, to ensure complete homogenisation, cells were incubated for 20 min in ice-containing cold water using an ultrasonic bath. All solvents and mixtures contained 0.01% (w/v) butylated hydroxytoluene (BHT). Lipids were then extracted using a modified protocol published by Lydic et al. (2014). In brief, 120 µl water (Milli-Q), 420 µl methanol and 220 µl chloroform were added to the homogenised cell pellet and mixed using the bullet blender. Samples were then centrifuged for 15 min at 20,000 ***g*** and supernatants collected into 2 ml safe-lock Eppendorf tubes. The pellets were re-extracted using 100 µl water and 400 µl methanol-chloroform mixture [2:1 (v/v)] and re-homogenised in the bullet blender for 30 s at speed 8. Subsequently, samples were centrifuged for 15 min at 20,000 ***g*** then the supernatants pooled with the previous extracts. The pooled supernatants were dried using a SpeedVac vacuum concentrator then reconstituted in 1 ml isopropanol:methanol: chloroform 4:2:1 (v/v/v) plus 0.01% (w/v) BHT.

nESI-FAIMS-UHRAMS analysis

100 µl of each lipid extract was dried in a 96-well plate (Eppendorf twin.tec PCR Plate 96, colourless) then reconstituted in 50 µl isopropanol:methanol: chloroform 4:2:1 (v/v/v) containing 0.5 mM sodium acetate. The plate was sealed with Teflon Ultra-Thin sealing tape (Analytical Sales and Services). Samples were introduced to an Orbitrap Fusion Lumos ultra-high resolution/ accurate mass spectrometer (Thermo Scientific) equipped with a Field Asymmetric Ion Mobility Spectrometry (FAIMS) interface (FAIMS Pro,

Thermo Scientific), using an Advion Triversa Nanomate nano electrospray ionisation (nESI) source (Advion). The nESI gas pressure was set to 0.3 psi and the spray voltage to 1.1 kV. The FAIMS Pro interface was operated in standard resolution mode using a compensation voltage of 60 V (optimised for the transmission of the $[M\text{-}2H]^{2-}$ precursor ion charge states of CL species using authentic standards). The Orbitrap Fusion Lumos ion transfer capillary temperature was set to 150°C, the RF-value to 10%, the AGC target to 2×10^5 and mass resolving power at 500,000 (at 200 *m*/*z*). Spectra were recorded in negative ionisation mode for a period of 3 min over a mass range of 350–1600 *m*/*z*.

Lipidomic data analysis

Mass spectrometry-based lipidome data was analysed using a developmental version of Lipid Search 5.0alpha software [Mitsui Knowledge Industry (MKI) and Thermo Fisher Scientific] with the following search parameters: Parent (mass) tolerance: 1.5 ppm, Correlation threshold (%): 0.3, Isotope threshold (%): 0.1, Max isotope number: 1, Parent threshold: 150, Recalc intensity threshold: 10, Peak detection was set to profile and merge mode to average. The spectra were mass calibrated using internal standards. Lipid 'sum composition' assignments were achieved using an accurate mass-based, user-defined database. Correction of ^{13}C isotope and automated peak finding was performed by the Lipid Search 5.0 alpha software. Lipid nomenclature used is in accordance with the LIPID MAPS consortium proposed naming scheme (Fahy et al., 2005, 2009). Semi-quantitative analysis of endogenous CL species was achieved by comparing the peak areas of identified lipids of interest to the peak area of the CL(14:0/14:0/14:0/14:0) internal standard (this lipid was first confirmed to not be present as an endogenous lipid in the samples) (Rustam and Reid, 2018).

Mitochondrial morphology imaging

Cells were seeded on 22×22 mm coverslips and allowed to attach overnight. Cells were incubated with 100 nM MitoTracker Orange (Molecular Probes, Thermo Fisher Scientific) in DMEM with no FBS for 15 min at 37°C. Alternatively, cells were transfected with 0.75 µg MRPL44–mCherry-containing plasmid to visualise the mitochondrial network, along with 1.75 µg of the experimental plasmid, and incubated for 72 h in normal growth conditions. Cells were then washed in DMEM, and fixed in 4% (w/v) paraformaldehyde in PBS for 30 min at room temperature. Cells were then mounted in DABCO in PVA medium (Sigma-Aldrich) and images were acquired with a DeltaVision fluorescent microscope (GE Healthcare) using a 60× objective 1.58 NA oil immersion objective. Images were acquired using a CoolSNAP HQ^2 CCD Camera. All images are presented as maximum projections of 0.2 µm optical sections and deconvolution was performed by softWoRx software (GE Healthcare). Mitochondrial morphology was qualitatively scored for 50 different cells from two independent slides and placed into one of four categories: elongated, where the majority of the mitochondrial network was interconnected and had a reticular appearance; mildly fragmented, where a minor section of the network is fragmented but the majority of the network had a reticular, interconnected appearance; moderately fragmented, where most of the network had a fragmented appearance but minor sections retain an interconnected structure; and highly fragmented, where the majority of the network was highly fragmented.

Gel electrophoresis

25 µg of isolated mitochondria from NIH-3T3 cells were separated on 4-12% Bis-Tris gels (Invitrogen) and samples were transferred onto a PVDF membrane (Bio-Rad). For Blue Native (BN)-PAGE, 80 µg of isolated mitochondria from NIH-3T3 cells were separated on 3–12% Bis-Tris native gels (Invitrogen) as previously described (Wittig et al., 2006).

Immunoblotting

Specific proteins were detected using mouse antibodies against total OXPHOS Cocktail (ab110412), COXII (ab198286), COXIII (ab110259) (Abcam, diluted 1:1000) and RFP (6G6) (Chromotek, diluted 1:1000); and rabbit antibodies against MRPL12 (HPA022853), MRPL34 (HPA042112) (Sigma-Prestige Antibodies, diluted 1:1000); MRPS35 (16457-1-AP), MRPL44 (16394-1-AP), MRPL45 (15682-1-AP), MRPS16 (16735-1-AP), OXA1 (21055-1-AP) (Proteintech, diluted 1:1000), Drp1 (D6C7) (8570S) (Cell Signaling, diluted 1:250), and GFP (Novus Biologicals, diluted 1:500) in 20% Odyssey blocking buffer (Li-COR Biosciences) in Tris-buffered saline and 0.05% (v/v) Tween 20 (TBST). IRDye 680LT goat anti-mouse-IgG and IRDye 800CW goat anti-rabbit-IgG secondary antibodies (Li-COR Biosciences, diluted 1:10,000) were used to detected primary antibodies. Blots were imaged using an Odyssey infrared imaging system (Li-COR Biosciences). Densitometry analysis was performed using ImageStudio and data is presented as mean±s.e.m. (n=3–6).

Mitochondrial protein synthesis

NIH-3T3 cells were seeded in six-well plates and allowed to attach overnight. *De novo* mitochondrial protein synthesis was measured as previously described (Davies et al., 2009). Growth medium was replaced with DMEM containing 10% FBS, 2 mg/ml glutamine and lacking methionine and cysteine, and cells were incubated for 30 min at 37°C. Following this, 100 µg/ml emetine was added and cells were incubated for 5 min. Then 200 µCi Express35S protein labelling mix [^{35}S] (Perkin Elmer) was added and cells were incubated for 1 h at 37°C. Cells were pelleted in ice-cold PBS, and 20 µg of protein was separated by 12.5% SDS-PAGE. Autoradiography signals were visualised on film. Equal loading was confirmed by Coomassie staining.

Respiration

Respiration was measured in digitonin-permeabilised NIH-3T3 cells, as previously described (Sanchez et al., 2011).

DNA extraction and mtDNA copy number quantitative PCR

NIH-3T3 cell DNA was extracted using a GeneJET Genomic DNA purification kit according to the manufacturer's instructions (Fermentas). Quantitative PCR was conducted on 100 ng of DNA using primers for cytochrome *b*, to determine levels of mitochondrial DNA, and primers for B2m, to determine levels of nuclear DNA (GeneWorks). Amplification was conducted using a Rotor-Gene Q (Qiagen) using SensiMix SYBR mix (Bioline). All primer sequences are listed in Table S1.

Sucrose gradient fractionation

Isolated mitochondria were separated on a 10–30% sucrose gradient as previously described (Rackham et al., 2016). Mitochondria were lysed in a buffer comprising 260 mM sucrose, 100 mM KCl, 20 mM $MgCl_2$, 10 mM Tris-HCl pH 7.5, 2% digitonin, 40 U/ml RNase inhibitor and 1× Complete protease inhibitor cocktail (Roche) for 20 min. Lysates were centrifuged at 9200 ***g*** for 45 min at 4°C, and clarified lysates were loaded on a continuous 10–30% sucrose gradient containing 100 mM KCl, 20 mM $MgCl_2$, 10 mM Tris-HCl pH 7.5 and aforementioned RNase and protease inhibitors. Lysates were centrifuged at 71,000 ***g*** in an Optima Beckman Coulter preparative ultracentrifuge. Fractions were collected and one-third of each fraction was precipitated with 0.02% sodium deoxycholate and 12% trichloroacetic acid, washed twice with acetone, and resolved by SDS-PAGE. Representative markers of the small and large ribosomal subunit were detected by immunoblotting as described above.

Live-cell imaging

NIH-3T3 cells were seeded onto a 35 mm glass-bottom Petri dish (MatTek) transfected with wild-type MRPL12 or MRPL44 with mCherry or GFP fused to the C termini in a pD2610-v10 mammalian expression vector (ATUM), as described above, and incubated for 72 h. Cells were stained with either 50 nM MitoTracker Green or 100 nM NAO 15 min prior to their respective experiments, and cells were washed three times with DMEM before imaging. Live-cell images were acquired on a Nikon A1Si spectral detector confocal system plus TIRF on a Nikon Ti-E inverted motorised microscope with a 60× water objective. Cells were incubated in a Tokai Hit stage top incubator (temperature-controlled chamber, 37°C, 5% CO_2) in combination with the Perfect Focus System (PFS) to prevent focus drift. Images were acquired by high-speed image capture using the Andor 885 EMCCD camera, all of which is controlled by the NIS Elements software.

All images were assembled and analysed using Fiji (NIH) (Schindelin et al., 2012). Scale bars represent 10 µm.

Variant calling

Adaptors were trimmed from the 5′ ends of sequenced reads with cutadapt v1.18 (Martin, 2011) and aligned with BBMap v37.02 (Bushnell et al., 2017) against the *Crls1* amplicon sequence. Duplicates were removed with samtools v1.7 (Li et al., 2009); rmdup and variants were called with freebayes v1.1.0-60-gc15b070 (Garrison and Marth, 2012 preprint), specifying a ploidy of 4 due to the tetraploidy of NIH-3T3 cells for chromosome 2 where the *Crls1* gene is located.

RNA sequencing and differential expression analysis

Adaptors were trimmed from the 5′ ends of sequenced reads with cutadapt (-O 1 -m 15) enforcing a minimum length of 15 nt, and read alignment was performed by Salmon v0.14.1 (Patro et al., 2017) (-l ISR –numBootstraps 1000 –seqBias –gcBias –validateMappings –mimicBT2) using the selective alignment procedure utilising a decoy-aware transcriptome index built from the GRCm38 reference sequence and customised GENCODE vM21 gene annotation. Differential gene expression analysis was performed with DESeq2 v1.24.0 (Love et al., 2014) and tximport v1.12.3 (Soneson et al., 2015), using apeglm v1.6.0 (Zhu et al., 2019) for log-fold change shrinkage. Gene ontology analysis was performed with DAVID v6.8 (Huang et al., 2009a,b) and visualised with REVIGO (Supek et al., 2011) and CirGO (Kuznetsova et al., 2019).

Super resolution microscopy

NIH-3T3 cells were transfected with wild-type mouse MRPL44, wild-type OXA1, or OXA1 without amino acids 332–433 (OXA1Δ332) (Integrated DNA Technologies) with mCherry or GFP fused to the C-termini in a pD2610-v10 mammalian expression vector as described above and incubated for 72 h. Where indicated, cells were treated with either vehicle (ethanol) or 100 µg/ml chloramphenicol for 4 h prior to experiments. Cells were fixed in 4% (w/v) paraformaldehyde in PBS for 20 min at room temperature, washed three times in 0.2% BSA-PBS, and mounted in ProLong Diamond Anti-fade medium (Invitrogen). Fixed cells were imaged on a Nikon SIM (Ti2) using Nikon SR Apo TIRF 100×1.49 NA oil immersion objective with motorised correction collar. Images are acquired on four colour platform (405 nm, 488 nm, 561 nm and 640 nm solid state lasers) and an Andor iXon 897 EMCCD camera, with NIS Elements software controlling confocal acquisition and lasers. Cells were excluded from analysis if they displayed signs of phototoxicity, such as blebbing or vacuolisation. All images were assembled and analysed using Fiji. Fluorescence intensities were analysed by Nikon NIS Elements software. Scale bars represent 10 µm. Inserts were taken from the area encompassed by the white rectangle and represent a sixfold enlargement of the boxed area with scale bars representing 2.5 µm. White lines on inserts are the area used for quantification analysis, with this area being represented on the *x*-axis of the quantification graph.

Immunoprecipitation

NIH-3T3 cells were transfected with MRPL12 with a GFP tag fused to the C-terminal end and either OXA1 with an mCherry tag fused to the C-terminal end or unfused mCherry in a pD2610-v10 mammalian expression vector, as described above, and incubated for 72 h. Cells were cross-linked in 2 mM dithiobis(succinimidyl propionate) (DSP; Life Technologies) in PBS for 30 min at room temperature followed by quenching in 50 mM glycine for 15 min. Cells were lysed in 260 mM sucrose, 100 mM KCl, 20 mM $MgCl_2$, 10 mM Tris-HCl pH 7.5, 1% digitonin, and complete EDTA-free protease inhibitor cocktail for 30 min at 4°C followed by sonication. Lysates were incubated with RFP-Trap anti-mCherry beads (Chromotek) for 2 h at 4°C. Beads were washed in digitonin-wash buffer (same components as lysis buffer except with 0.1% digitonin), washed again in IGEPAL-wash buffer [same components as lysis buffer except with 1% IGEPAL CA-630 (Sigma)], then eluted in 2× SDS-PAGE sample buffer by heating at 95°C for 10 min. 5 µl of input samples, taken immediately after lysis, and the entire final elution samples, were run on SDS-PAGE gels, and analysed by immunoblotting as described above.

BiFC assay

NIH-3T3 cells were transfected with separate plasmids encoding MRPL44 or OXA1 with the VN fragment (amino acids 1–173 of Venus) attached to the C terminal end, and MRPL44 or OXA1 with the VC fragment (amino acids 174–239 of Venus) attached to the C terminal end, and mCherry RFP in a 2:2:1 ratio as described above. At 72 h post transfection, cells were trypsinised, resuspended in PBS plus 2% FBS, and analysed by FACS using a FACS Aria BDII. RFP was used as a marker of transfected cells, and cells transfected with RFP only, or transfected with an empty vector in place of the VN- and VC-tagged proteins, were analysed to determine GFP background intensity. The RFP signal was used to identify transfected cells, and the Venus signal was quantified and normalised to the RFP signal of transfected cells. The Venus-positive cells are indicative of the interactions between the two proteins investigated, where the number of Venus-positive cells indicates the frequency of interactions, and the intensity of Venus fluorescence indicates the strength of the interaction. The average GFP intensity, and number of GFP-positive cells present in the transfected cell population was averaged between three independent transfections. For average intensity analysis, GFP background was subtracted from the sample GFP geometric mean, and then divided by the geometric mean of RFP in the GFP-positive population. This was then expressed as a relative change compared to the respective control. For ethanol and chloramphenicol treatment experiments, samples were incubated with either 100 µg/ml chloramphenicol in ethanol or ethanol alone throughout all stages of the experiment and data acquisition.

Statistical analysis

All data is displayed as mean±s.d. or s.e.m., and statistical significance was calculated using a two-tailed Student's *t*-test.

Acknowledgements

We thank Professor Nenad Ban and Dr Eva Kummer for helpful discussions and advice. We also thank Dr Ji Li for assisting with FACS, and Thermo Fisher Scientific for providing the FAIMS-Pro interface as part of a collaborative research agreement with G.E.R.

Competing interests

The authors declare no competing or financial interests.

Author contributions

Conceptualization: O.R., A.F.; Methodology: R.G.L., S.J.S., A.-M.S., G.E.R., O.R., A.F.; Validation: R.G.L., S.J.S., J.A.E., V.H., J.C.M., G.E.R., A.F.; Formal analysis: R.G.L., J.G., S.J.S., A.-M.S., J.A.E., V.H., J.C.M., G.E.R., A.F.; Investigation: R.G.L., J.G., S.J.S., A.-M.S., J.A.E., G.E.R., A.F.; Resources: G.E.R., O.R., A.F.; Writing - original draft: R.G.L., S.J.S., O.R., A.F.; Writing - review & editing: R.G.L., J.G., S.J.S., A.-M.S., J.A.E., V.H., J.C.M., M.Z., G.E.R., O.R., A.F.; Visualization: R.G.L., J.G., S.J.S., J.C.M., G.E.R., A.F.; Supervision: M.Z., G.E.R., O.R., A.F.; Project administration: A.F.; Funding acquisition: G.E.R., O.R., A.F.

Funding

This project was supported by fellowships and project grants from the National Health and Medical Research Council (APP1058442, APP1045677, APP1041582, APP1023460, APP1005030, APP1043978 to A.F. and O.R.), the Australian Research Council (DP180101656 to A.F. and O.R. and DP190102464 to G.E.R.), the Cancer Council of Western Australia (to O.R. and A.F.). R.G.L. and J.C.M. are supported by UWA Postgraduate Scholarships and J.G. by a Perron Fellowship.

Data availability

The RNA-seq data for this paper have been deposited in the Gene Expression Omnibus (GEO) under accession number GSE148178.

Supplementary information

Supplementary information available online at
https://jcs.biologists.org/lookup/doi/10.1242/jcs.240374.supplemental

References

Almajan, E. R., Richter, R., Paeger, L., Martinelli, P., Barth, E., Decker, T., Larsson, N.-G., Kloppenburg, P., Langer, T. and Rugarli, E. I. (2012). AFG3L2 supports mitochondrial protein synthesis and Purkinje cell survival. *J. Clin. Invest.* **122**, 4048-4058. doi:10.1172/JCI64604

Antonicka, H. and Shoubridge, E. A. (2015). Mitochondrial RNA granules are centers for posttranscriptional RNA processing and ribosome biogenesis. *Cell Rep.* **10**, 920-932. doi:10.1016/j.celrep.2015.01.030

Ban, T., Kohno, H., Ishihara, T. and Ishihara, N. (2018). Relationship between OPA1 and cardiolipin in mitochondrial inner-membrane fusion. *Biochim. Biophys. Acta BBA Bioenerg.* **1859**, 951-957. doi:10.1016/j.bbabio.2018.05.016

Barth, P. G., Scholte, H. R., Berden, J. A., Van Der Klei-Van Moorsel, J. M., Luyt-Houwen, I. E. M., Van'T Veer-Korthof, E. T., Van Der Harten, J. J. and Sobotka-Plojhar, M. A. (1983). An X-linked mitochondrial disease affecting cardiac muscle, skeletal muscle and neutrophil leucocytes. *J. Neurol. Sci.* **62**, 327-355. doi:10.1016/0022-510X(83)90209-5

Bogenhagen, D. F., Martin, D. W. and Koller, A. (2014). Initial steps in RNA processing and ribosome assembly occur at mitochondrial DNA nucleoids. *Cell Metab.* **19**, 618-629. doi:10.1016/j.cmet.2014.03.013

Bushnell, B., Rood, J. and Singer, E. (2017). BBMerge – Accurate paired shotgun read merging via overlap. *PLoS ONE* **12**, e0185056. doi:10.1371/journal.pone.0185056

Cámara, Y., Asin-Cayuela, J., Park, C. B., Metodiev, M. D., Shi, Y., Ruzzenente, B., Kukat, C., Habermann, B., Wibom, R., Hultenby, K. et al. (2011). MTERF4 regulates translation by targeting the methyltransferase NSUN4 to the mammalian mitochondrial ribosome. *Cell Metab.* **13**, 527-539. doi:10.1016/j.cmet.2011.04.002

Chen, D., Zhang, X.-Y. and Shi, Y. (2006). Identification and functional characterization of hCLS1, a human cardiolipin synthase localized in mitochondria. *Biochem. J.* **398**, 169-176. doi:10.1042/BJ20060303

Claypool, S. M. and Koehler, C. M. (2012). The complexity of cardiolipin in health and disease. *Trends Biochem. Sci.* **37**, 32-41. doi:10.1016/j.tibs.2011.09.003

Cogliati, S., Enriquez, J. A. and Scorrano, L. (2016). Mitochondrial cristae: where beauty meets functionality. *Trends Biochem. Sci.* **41**, 261-273. doi:10.1016/j.tibs.2016.01.001

Davies, S. M. K., Rackham, O., Shearwood, A.-M. J., Hamilton, K. L., Narsai, R., Whelan, J. and Filipovska, A. (2009). Pentatricopeptide repeat domain protein 3 associates with the mitochondrial small ribosomal subunit and regulates translation. *FEBS Lett.* **583**, 1853-1858. doi:10.1016/j.febslet.2009.04.048

Dudek, J. (2017). Role of cardiolipin in mitochondrial signaling pathways. *Front. Cell Dev. Biol.* **5**, 90. doi:10.3389/fcell.2017.00090

Dudkina, N. V., Kudryashev, M., Stahlberg, H. and Boekema, E. J. (2011). Interaction of complexes I, III, and IV within the bovine respirasome by single particle cryoelectron tomography. *Proc. Natl. Acad. Sci. USA* **108**, 15196-15200. doi:10.1073/pnas.1107819108

Duff, R. M., Shearwood, A.-M. J., Ermer, J., Rossetti, G., Gooding, R., Richman, T. R., Balasubramaniam, S., Thorburn, D. R., Rackham, O., Lamont, P. J. et al. (2015). A mutation in MT-TW causes a tRNA processing defect and reduced mitochondrial function in a family with Leigh syndrome. *Mitochondrion* **25**, 113-119. doi:10.1016/j.mito.2015.10.008

Fahy, E., Subramaniam, S., Brown, H. A., Glass, C. K., Merrill, A. H., Murphy, R. C., Raetz, C. R. H., Russell, D. W., Seyama, Y., Shaw, W. et al. (2005). A comprehensive classification system for lipids. *J. Lipid Res.* **46**, 839-862. doi:10.1194/jlr.E400004-JLR200

Fahy, E., Subramaniam, S., Murphy, R. C., Nishijima, M., Raetz, C. R. H., Shimizu, T., Spener, F., van Meer, G., Wakelam, M. J. O. and Dennis, E. A. (2009). Update of the LIPID MAPS comprehensive classification system for lipids. *J. Lipid Res.* **50**, S9-S14. doi:10.1194/jlr.R800095-JLR200

Ferreira, N., Perks, K. L., Rossetti, G., Rudler, D. L., Hughes, L. A., Ermer, J. A., Scott, L. H., Kuznetsova, I., Richman, T. R., Narayana, V. K. et al. (2019). Stress signaling and cellular proliferation reverse the effects of mitochondrial mistranslation. *EMBO J.* **38**, e102155. doi:10.15252/embj.2019102155

Garrison, E. and Marth, G. (2012). Haplotype-based variant detection from short-read sequencing. *ArXiv12073907 Q-Bio*. https://arxiv.org/abs/1207.3907

Genova, M. L. and Lenaz, G. (2014). Functional role of mitochondrial respiratory supercomplexes. *Biochim. Biophys. Acta BBA Bioenerg.* **1837**, 427-443. doi:10.1016/j.bbabio.2013.11.002

Gonzalvez, F., D'Aurelio, M., Boutant, M., Moustapha, A., Puech, J.-P., Landes, T., Arnauné-Pelloquin, L., Vial, G., Taleux, N., Slomianny, C. et al. (2013). Barth syndrome: cellular compensation of mitochondrial dysfunction and apoptosis inhibition due to changes in cardiolipin remodeling linked to tafazzin (TAZ) gene mutation. *Biochim. Biophys. Acta BBA Mol. Basis Dis.* **1832**, 1194-1206. doi:10.1016/j.bbadis.2013.03.005

Greber, B. J., Boehringer, D., Leibundgut, M., Bieri, P., Leitner, A., Schmitz, N., Aebersold, R. and Ban, N. (2014). The complete structure of the large subunit of the mammalian mitochondrial ribosome. *Nature* **515**, 283-286. doi:10.1038/nature13895

Han, J., Back, S. H., Hur, J., Lin, Y.-H., Gildersleeve, R., Shan, J., Yuan, C. L., Krokowski, D., Wang, S., Hatzoglou, M. et al. (2013). ER-stress-induced transcriptional regulation increases protein synthesis leading to cell death. *Nat. Cell Biol.* **15**, 481-490. doi:10.1038/ncb2738

Haque, M. E., Elmore, K. B., Tripathy, A., Koc, H., Koc, E. C. and Spremulli, L. L. (2010a). Properties of the C-terminal tail of human mitochondrial inner membrane protein Oxa1L and its interactions with mammalian mitochondrial ribosomes. *J. Biol. Chem.* **285**, 28353-28362. doi:10.1074/jbc.M110.148262

Haque, M. E., Spremulli, L. L. and Fecko, C. J. (2010b). Identification of protein-protein and protein-ribosome interacting regions of the C-terminal tail of human mitochondrial inner membrane protein Oxa1L. *J. Biol. Chem.* **285**, 34991-34998. doi:10.1074/jbc.M110.163808

Houtkooper, R. H. and Vaz, F. M. (2008). Cardiolipin, the heart of mitochondrial metabolism. *Cell. Mol. Life Sci. CMLS* **65**, 2493-2506. doi:10.1007/s00018-008-8030-5

Huang, D. W., Sherman, B. T. and Lempicki, R. A. (2009a). Systematic and integrative analysis of large gene lists using DAVID bioinformatics resources. *Nat. Protoc.* **4**, 44-57. doi:10.1038/nprot.2008.211

Huang, D. W., Sherman, B. T. and Lempicki, R. A. (2009b). Bioinformatics enrichment tools: paths toward the comprehensive functional analysis of large gene lists. *Nucleic Acids Res.* **37**, 1-13. doi:10.1093/nar/gkn923

Jourdain, A. A., Boehm, E., Maundrell, K. and Martinou, J.-C. (2016). Mitochondrial RNA granules: compartmentalizing mitochondrial gene expression. *J. Cell Biol.* **212**, 611-614. doi:10.1083/jcb.201507125

Kühlbrandt, W. (2015). Structure and function of mitochondrial membrane protein complexes. *BMC Biol.* **13**, 89. doi:10.1186/s12915-015-0201-x

Kummer, E., Leibundgut, M., Rackham, O., Lee, R. G., Boehringer, D., Filipovska, A. and Ban, N. (2018). Unique features of mammalian mitochondrial translation initiation revealed by cryo-EM. *Nature* **560**, 263-267. doi:10.1038/s41586-018-0373-y

Kuznetsova, I., Lugmayr, A., Siira, S. J., Rackham, O. and Filipovska, A. (2019). CirGO: an alternative circular way of visualising gene ontology terms. *BMC Bioinformatics* **20**, 84. doi:10.1186/s12859-019-2671-2

Lee, R. G., Rudler, D. L., Rackham, O. and Filipovska, A. (2018). Is mitochondrial gene expression coordinated or stochastic? *Biochem. Soc. Trans.* **46**, 1239-1246. doi:10.1042/BST20180174

Li, H., Handsaker, B., Wysoker, A., Fennell, T., Ruan, J., Homer, N., Marth, G., Abecasis, G., Durbin, R. and **1000 Genome Project Data Processing Subgroup** (2009). The Sequence Alignment/Map format and SAMtools. *Bioinforma. Oxf. Engl.* **25**, 2078-2079. doi:10.1093/bioinformatics/btp352

Li, J., Romestaing, C., Han, X., Li, Y., Hao, X., Wu, Y., Sun, C., Liu, X., Jefferson, L. S., Xiong, J. et al. (2010). Cardiolipin remodeling by ALCAT1 links oxidative stress and mitochondrial dysfunction to obesity. *Cell Metab.* **12**, 154-165. doi:10.1016/j.cmet.2010.07.003

Li, J., Liu, X., Wang, H., Zhang, W., Chan, D. C. and Shi, Y. (2012). Lysocardiolipin acyltransferase 1 (ALCAT1) controls mitochondrial DNA fidelity and biogenesis through modulation of MFN2 expression. *Proc. Natl. Acad. Sci. USA* **109**, 6975-6980. doi:10.1073/pnas.1120043109

Love, M. I., Huber, W. and Anders, S. (2014). Moderated estimation of fold change and dispersion for RNA-seq data with DESeq2. *Genome Biol.* **15**, 550. doi:10.1186/s13059-014-0550-8

Lydic, T. A., Busik, J. V. and Reid, G. E. (2014). A monophasic extraction strategy for the simultaneous lipidome analysis of polar and nonpolar retina lipids. *J. Lipid Res.* **55**, 1797-1809. doi:10.1194/jlr.D050302

Martin, M. (2011). Cutadapt removes adapter sequences from high-throughput sequencing reads. *EMBnet.journal* **17**, 10-12. doi:10.14806/ej.17.1.200

Metodiev, M. D., Spåhr, H., Polosa, P. L., Meharg, C., Becker, C., Altmueller, J., Habermann, B., Larsson, N.-G. and Ruzzenente, B. (2014). NSUN4 is a dual function mitochondrial protein required for both methylation of 12S rRNA and coordination of mitoribosomal assembly. *PLoS Genet.* **10**, e1004110. doi:10.1371/journal.pgen.1004110

Miklas, J. W., Clark, E., Levy, S., Detraux, D., Leonard, A., Beussman, K., Showalter, M. R., Smith, A. T., Hofsteen, P., Yang, X. et al. (2019). TFPa/HADHA is required for fatty acid beta-oxidation and cardiolipin re-modeling in human cardiomyocytes. *Nat. Commun.* **10**, 1-21. doi:10.1038/s41467-019-12482-1

Morell, M., Espargaro, A., Aviles, F. X. and Ventura, S. (2008). Study and selection of in vivo protein interactions by coupling bimolecular fluorescence complementation and flow cytometry. *Nat. Protoc.* **3**, 22-33. doi:10.1038/nprot.2007.496

Mourier, A., Ruzzenente, B., Brandt, T., Kühlbrandt, W. and Larsson, N.-G. (2014). Loss of LRPPRC causes ATP synthase deficiency. *Hum. Mol. Genet.* **23**, 2580-2592. doi:10.1093/hmg/ddt652

Nargang, F. E., Preuss, M., Neupert, W. and Herrmann, J. M. (2002). The Oxa1 Protein forms a homooligomeric complex and is an essential part of the mitochondrial export translocase in neurospora crassa. *J. Biol. Chem.* **277**, 12846-12853. doi:10.1074/jbc.M112099200

Osman, C., Voelker, D. R. and Langer, T. (2011). Making heads or tails of phospholipids in mitochondria. *J. Cell Biol.* **192**, 7-16. doi:10.1083/jcb.201006159

Otera, H., Miyata, N., Kuge, O. and Mihara, K. (2016). Drp1-dependent mitochondrial fission via MiD49/51 is essential for apoptotic cristae remodeling. *J. Cell Biol.* **212**, 531-544. doi:10.1083/jcb.201508099

Ott, M. and Herrmann, J. M. (2010). Co-translational membrane insertion of mitochondrially encoded proteins. *Biochim. Biophys. Acta* **1803**, 767-775. doi:10.1016/j.bbamcr.2009.11.010

Paradies, G., Paradies, V., De Benedictis, V., Ruggiero, F. M. and Petrosillo, G. (2014). Functional role of cardiolipin in mitochondrial bioenergetics. *Biochim. Biophys. Acta BBA Bioenerg.* **1837**, 408-417. doi:10.1016/j.bbabio.2013.10.006

Patro, R., Duggal, G., Love, M. I., Irizarry, R. A. and Kingsford, C. (2017). Salmon provides fast and bias-aware quantification of transcript expression. *Nat. Methods* **14**, 417-419. doi:10.1038/nmeth.4197

Perks, K. L., Ferreira, N., Richman, T. R., Ermer, J. A., Kuznetsova, I., Shearwood, A.-M. J., Lee, R. G., Viola, H. M., Johnstone, V. P. A., Matthews, V. et al. (2017). Adult-onset obesity is triggered by impaired mitochondrial gene expression. *Sci. Adv.* **3**, e1700677. doi:10.1126/sciadv.1700677

Perks, K. L., Rossetti, G., Kuznetsova, I., Hughes, L. A., Ermer, J. A., Ferreira, N., Busch, J. D., Rudler, D. L., Spahr, H., Schöndorf, T. et al. (2018). PTCD1 is required for 16S rRNA maturation complex stability and mitochondrial ribosome assembly. *Cell Rep.* **23**, 127-142. doi:10.1016/j.celrep.2018.03.033

Petit, J.-M., Maftah, A., Ratinaud, M.-H. and Julien, R. (1992). 10N-Nonyl acridine orange interacts with cardiolipin and allows the quantification of this phospholipid in isolated mitochondria. *Eur. J. Biochem.* **209**, 267-273. doi:10.1111/j.1432-1033.1992.tb17285.x

Pfleger, J., He, M. and Abdellatif, M. (2015). Mitochondrial complex II is a source of the reserve respiratory capacity that is regulated by metabolic sensors and promotes cell survival. *Cell Death Dis.* **6**, e1835. doi:10.1038/cddis.2015.202

Preuss, M., Leonhard, K., Hell, K., Stuart, R. A., Neupert, W. and Herrmann, J. M. (2001). Mba1, a novel component of the mitochondrial protein export machinery of the yeast Saccharomyces cerevisiae. *J. Cell Biol.* **153**, 1085-1095. doi:10.1083/jcb.153.5.1085

Rackham, O., Davies, S. M. K., Shearwood, A.-M. J., Hamilton, K. L., Whelan, J. and Filipovska, A. (2009). Pentatricopeptide repeat domain protein 1 lowers the levels of mitochondrial leucine tRNAs in cells. *Nucleic Acids Res.* **37**, 5859-5867. doi:10.1093/nar/gkp627

Rackham, O., Busch, J. D., Matic, S., Siira, S. J., Kuznetsova, I., Atanassov, I., Ermer, J. A., Shearwood, A.-M. J., Richman, T. R., Stewart, J. B. et al. (2016). Hierarchical RNA processing is required for mitochondrial ribosome assembly. *Cell Rep.* **16**, 1874-1890. doi:10.1016/j.celrep.2016.07.031

Richman, T. R., Rackham, O. and Filipovska, A. (2014). Mitochondria: unusual features of the mammalian mitoribosome. *Int. J. Biochem. Cell Biol.* **53**, 115-120. doi:10.1016/j.biocel.2014.05.011

Rustam, Y. H. and Reid, G. E. (2018). Analytical challenges and recent advances in mass spectrometry based lipidomics. *Anal. Chem.* **90**, 374-397. doi:10.1021/acs.analchem.7b04836

Ryan, T., Bamm, V. V., Stykel, M. G., Coackley, C. L., Humphries, K. M., Jamieson-Williams, R., Ambasudhan, R., Mosser, D. D., Lipton, S. A., Harauz, G. et al. (2018). Cardiolipin exposure on the outer mitochondrial membrane modulates α-synuclein. *Nat. Commun.* **9**, 817. doi:10.1038/s41467-018-03241-9

Sakamoto, T., Inoue, T., Otomo, Y., Yokomori, N., Ohno, M., Arai, H. and Nakagawa, Y. (2012). Deficiency of cardiolipin synthase causes abnormal mitochondrial function and morphology in germ cells of Caenorhabditis elegans. *J. Biol. Chem.* **287**, 4590-4601. doi:10.1074/jbc.M111.314823

Sanchez, M. I. G. L., Mercer, T. R., Davies, S. M. K., Shearwood, A.-M. J., Nygård, K. K. A., Richman, T. R., Mattick, J. S., Rackham, O. and Filipovska, A. (2011). RNA processing in human mitochondria. *Cell Cycle* **10**, 2904-2916. doi:10.4161/cc.10.17.17060

Schenkel, L. C. and Bakovic, M. (2014). Formation and regulation of mitochondrial membranes. *Int. J. Cell Biol.* **2014**, 13. doi:10.1155/2014/709828

Schindelin, J., Arganda-Carreras, I., Frise, E., Kaynig, V., Longair, M., Pietzsch, T., Preibisch, S., Rueden, C., Saalfeld, S., Schmid, B. et al. (2012). Fiji: an open-source platform for biological-image analysis. *Nat. Methods* **9**, 676-682. doi:10.1038/nmeth.2019

Soneson, C., Love, M. I. and Robinson, M. D. (2015). Differential analyses for RNA-seq: transcript-level estimates improve gene-level inferences. *F1000Research* **4**, 1521. doi:10.12688/f1000research.7563.1

Song, C., Zhang, J., Qi, S., Liu, Z., Zhang, X., Zheng, Y., Andersen, J.-P., Zhang, W., Strong, R., Martinez, P. A. et al. (2019). Cardiolipin remodeling by ALCAT1 links mitochondrial dysfunction to Parkinson's diseases. *Aging Cell* **18**, e12941. doi:10.1111/acel.12941

Soustek, M. S., Falk, D. J., Mah, C. S., Toth, M. J., Schlame, M., Lewin, A. S. and Byrne, B. J. (2010). Characterization of a transgenic short hairpin RNA-induced murine model of tafazzin deficiency. *Hum. Gene Ther.* **22**, 865-871. doi:10.1089/hum.2010.199

Supek, F., Bošnjak, M., Škunca, N. and Šmuc, T. (2011). REVIGO summarizes and visualizes long lists of gene ontology terms. *PLOS ONE* **6**, e21800. doi:10.1371/journal.pone.0021800

Sustarsic, E. G., Ma, T., Lynes, M. D., Larsen, M., Karavaeva, I., Havelund, J. F., Nielsen, C. H., Jedrychowski, M. P., Moreno-Torres, M., Lundh, M. et al. (2018). Cardiolipin synthesis in brown and beige fat mitochondria is essential for systemic energy homeostasis. *Cell Metab.* **28**, 159-174.e11. doi:10.1016/j.cmet.2018.05.003

Taylor, W. A. and Hatch, G. M. (2009). Identification of the human mitochondrial Linoleoyl-coenzyme a monolysocardiolipin acyltransferase (MLCL AT-1). *J. Biol. Chem.* **284**, 30360-30371. doi:10.1074/jbc.M109.048322

Thompson, K., Mai, N., Oláhová, M., Scialó, F., Formosa, L. E., Stroud, D. A., Garrett, M., Lax, N. Z., Robertson, F. M., Jou, C. et al. (2018). OXA1L mutations cause mitochondrial encephalopathy and a combined oxidative phosphorylation defect. *EMBO Mol. Med.* **10**, e9060. doi:10.15252/emmm.201809060

Vafai, S. B. and Mootha, V. K. (2012). Mitochondrial disorders as windows into an ancient organelle. *Nature* **491**, 374-383. doi:10.1038/nature11707

Wang, L. and Carnegie, G. K. (2013). Flow cytometric analysis of bimolecular fluorescence complementation: a high throughput quantitative method to study protein-protein interaction. *J. Vis. Exp. JoVE* **15**, 50529. doi:10.3791/50529

Weiss, C., Oppliger, W., Vergères, G., Demel, R., Jenö, P., Horst, M., Kruijff, B. de, Schatz, G. and Azem, A. (1999). Domain structure and lipid interaction of recombinant yeast Tim44. *Proc. Natl. Acad. Sci. USA* **96**, 8890-8894. doi:10.1073/pnas.96.16.8890

Wittig, I., Braun, H.-P. and Schägger, H. (2006). Blue native PAGE. *Nat. Protoc.* **1**, 418-428. doi:10.1038/nprot.2006.62

Xu, Y., Malhotra, A., Ren, M. and Schlame, M. (2006). The enzymatic function of tafazzin. *J. Biol. Chem.* **281**, 39217-39224. doi:10.1074/jbc.M606100200

Zhu, A., Ibrahim, J. G. and Love, M. I. (2019). Heavy-tailed prior distributions for sequence count data: removing the noise and preserving large differences. *Bioinforma. Oxf. Engl.* **35**, 2084-2092. doi:10.1093/bioinformatics/bty895